Acta Materialia 249 (2023) 118831

Contents lists available at ScienceDirect

Acta Materialia

journal homepage: www.elsevier.com/locate/actamat

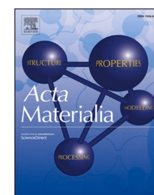

Full length article

Nucleation and growth of Ag_3Sn in Sn-Ag and Sn-Ag-Cu solder alloys

Y. Cui [a], J.W. Xian [a,*], A. Zois [a], K. Marquardt [a], H. Yasuda [b], C.M. Gourlay [a]

[a] Department of Materials, Imperial College London, London. SW7 2AZ. UK

[b] Department of Materials Science & Engineering, Kyoto University, Sakyo-ku, Kyoto, 606-8501, Japan

ARTICLE INFO

Keywords:
Soldering
Undercooling
Solidification
Synchrotron radiation
Intermetallic compounds (IMCs)

ABSTRACT

Large Ag_3Sn plates in solder joints can affect the reliability of electronics, however, the factors affecting their nucleation and morphology are not well understood. Here, the faceted solidification of Ag_3Sn was studied as a function of melt undercooling, revealing transitions from single crystal {001} plates to cyclic twinned plates and then to highly branched structures created by twin mediated branching. Real-time X-ray imaging proved that Ag_3Sn cyclic twins come from a common point, indicating they initiate in the process of nucleation or in the very early stages of growth in the undercooled melt. Soldering to copper substrates significantly catalysed Ag_3Sn nucleation. This is shown to be due to constitutional supercooling generated by Ag solute rejection into the liquid ahead of the Cu_6Sn_5 reaction layer, with additional contributions from geometrical catalysis in the grooves between Cu_6Sn_5 scallops and heterogeneous nucleation of Ag_3Sn on Cu_6Sn_5. The relative ease of Ag_3Sn nucleation on the Cu_6Sn_5 reaction layer is responsible for the large plates often reported in electronic solder joints.

1. Introduction

Silver is a key component in many electronic solder alloys. In the era of leaded solders, Sn-3.5Ag was used in applications where Sn-37 Pb was unsuitable including when soldering to thick-film silver conductors. During the transition to Pb-free solders, the use of Sn-3.5Ag has continued and new Ag-containing solders have become widespread, often based on Sn-Ag-Cu (SAC) compositions due to the ubiquity of copper substrates. These include the first generation Pb-free solders SAC387 and SAC305 [1,2], the second generation alloys SAC0307 and SAC105 [3–5], and emerging third generation alloys which typically add Bi and/or Sb to near-eutectic Sn-Ag-Cu compositions [6–9]. In all these solders, the intermetallic compound (IMC) Ag_3Sn forms during solidification in a eutectic reaction and, sometimes, also as a primary solidification phase. Since all these solders are eutectic or hypoeutectic compositions, the formation of primary Ag_3Sn occurs when the liquid supercools with respect to the β-Sn liquidus due to nucleation difficulties of the β-Sn phase [10–12].

Extensive work has explored the formation of eutectic Ag_3Sn and three types of morphologies have been identified: plate-like, needle-like and spheroidal Ag_3Sn. One body of work has applied unidirectional solidification under controlled conditions to show that there is a plate to rod eutectic growth transition with increasing growth velocity [13–17]. Another body of work has shown that cooling rate in castings and solder joints [18–22] plays a significant role in the size and morphology of Ag_3Sn: a fine distribution of spheroidal Ag_3Sn particles was observed at higher cooling rate (17∼24 °C/s) while coarse needle-like and plate-like Ag_3Sn were formed at low cooling rate (∼0.1 °C/s). Increasing the volume fraction of eutectic Ag_3Sn provides enhanced strength [23] and improves resistance to creep and thermal fatigue [24–28], and a finer eutectic Ag_3Sn lengthscale improves creep resistance further [29,30].

The role of primary Ag_3Sn plates on solder joint reliability is less clear than for eutectic Ag_3Sn. Some investigators found large primary Ag_3Sn to be detrimental to mechanical performance [11,31-33]. Other studies have indicated that the role of large Ag_3Sn plates depends on their location in the joint: they are detrimental when aligned in the direction of crack propagation, whereas large plates can enhance thermal fatigue life when aligned such that they block or arrest an advancing crack [34]. An additional factor is that the solubility of Ag is negligible in the β-Sn and Cu_6Sn_5 phases [35]. Thus, almost all Ag atoms go into Ag_3Sn and the formation of primary Ag_3Sn ties up Ag atoms that would otherwise form small eutectic Ag_3Sn [36], reducing the volume fraction of effective strengthening particles.

Prior work has focussed on finding ways to prevent the formation of primary Ag_3Sn plates [37–39]. Reducing the Ag content in the alloy is a simple method to prevent their formation; with a silver content less than 3 wt.% in SAC alloys large Ag_3Sn formation can be substantially reduced even under extremely slow cooling conditions (0.02 °C/s) [37].

* Corresponding author.
E-mail address: j.xian@imperial.ac.uk (J.W. Xian).

https://doi.org/10.1016/j.actamat.2023.118831
Received 6 October 2022; Received in revised form 15 February 2023; Accepted 5 March 2023
Available online 6 March 2023
1359-6454/© 2023 The Authors. Published by Elsevier Ltd on behalf of Acta Materialia Inc. This is an open access article under the CC BY license (http://creativecommons.org/licenses/by/4.0/).

However, Ag contents of 3 wt.% or higher may be desirable for performance in thermal cycling [5]. Primary Ag_3Sn can also be reduced or completely supressed at sufficiently high cooling rate in freestanding solder balls with near-eutectic ternary Sn-Ag-Cu composition [37,38], although there is often limited scope for altering the cooling rate in a soldering process. Since primary Ag_3Sn forms as the liquid supercools with respect to the β-Sn liquidus, primary Ag_3Sn plates can also be suppressed by additions that promote the nucleation of the β-Sn phase [39]. For example, Kang et al. [38] demonstrated that dilute Zn additions to Sn-3.8Ag-0.7Cu reduce the undercooling for β-Sn and prevent Ag_3Sn formation in alloys with near-eutectic Ag content and low cooling rate (0.02 °C/s).

For Sn-Ag-Cu solders, primary Ag_3Sn typically grows with a faceted plate morphology [12,40-43]. Kim et al. [40] observed Ag_3Sn plates at the top of the interfacial reaction layer with different growth stages varying from faceted dendrites to hopper crystals and simple plate morphologies in Sn-3.9Ag-0.6Cu solder joints. Gong et al. [42] reported that Ag_3Sn plates in Sn-3.8Ag-0.7Cu/Cu joints nucleate preferably near the solder/substrate interface. Through in-situ synchrotron X-ray imaging of Sn-3.5Ag/Cu joints, Ma et al. [44] proposed three growth patterns for Ag_3Sn plates: linear, Y and X shape. It was interpreted later by Mueller et al. [45] that the multiplate formations do not necessarily develop into all six directions. Mueller et al. [45] also observed star-shaped Ag_3Sn morphology in Sn-5Ag solders which they attributed to its pseudo-hexagonal structure with the main plate facet and two perpendicular in-plane growth directions indexed using a hexagonal unit cell. However, the detailed mechanisms affecting the formation of these Ag_3Sn morphologies remain ambiguous, and the difference in Ag_3Sn nucleation and growth between freestanding balls and solder joints is also unclear.

This work was conducted to build a deeper understanding of the nucleation and growth of primary Ag_3Sn crystals in solder balls and in joints on Cu substrates. We first study binary Sn-Ag solder balls and focus on (i) the nucleation undercooling for Ag_3Sn, (ii) the Ag_3Sn nucleation location, and (iii) the influence of melt undercooling on the growth of Ag_3Sn crystals. We then explore how factors (i)-(iii) are affected by the presence of Cu solute, pre-existing Cu_6Sn_5 primary crystals, a Cu_6Sn_5 reaction layer, and the nucleation of β-Sn.

2. Methods

2.1. Sample preparation

Sn-5Ag, Sn-3.5Ag, Sn-3Ag-0.5Cu, Sn-3Ag-1Cu and Sn-4Ag-0.5Cu (wt.%) alloys were made by melting 99.999% Sn with 99.9% Ag and Sn-10 wt.% Cu master alloy. The mixture was heated to 300 °C in a clay-bonded graphite crucible in a resistance furnace. After holding for 2 h, the melt was stirred with an Al_2O_3 rod and then poured into a steel mould. Alloys were rolled to ~30 μm foils, punched into Ø 1.6 mm discs and reflowed in a ROL-1 tacky flux on a hotplate at 280 °C to form ~500 μm diameter spheres due to surface tension. The balls were then used in one of three forms: (i) as freestanding balls, (ii) as single balls soldered to a copper substrate on one side, or (iii) as a 2 × 2 ball array joining copper to copper.

2.2. Differential scanning calorimetry (DSC)

To apply controlled cooling conditions and measure the nucleation temperature of the Ag_3Sn and β-Sn phases, the 500 μm balls and joints were melted and solidified in a Mettler Toledo DSC in aluminium pans under a nitrogen atmosphere. The standard reflow profile used was to heat to a peak temperature of 280 °C for Sn-5Ag and 230 °C for all other solder compositions, hold for 10 min, and then cool at a rate of 5 K/min. >20 samples were studied for each composition. In Sn-5Ag, >80 samples were studied to obtain data on the distribution of undercoolings and to explore the undercooling-microstructure relationship for primary Ag_3Sn over a wide range.

Table 1
Crystal structures of Ag_3Sn and Cu_6Sn_5 assumed in this work.

Crystals	Space group	Pearson symbol	Lattice parameters	Ref.
Ag_3Sn	PmmnZ	*oP8*	a = 4.7823 Å, b = 5.9975 Å, c = 5.1639Å	[52]
Cu_6Sn_5	$P6_3$/mmc	*hP4*	a = 4.1920 Å, b = 4.1920 Å, c = 5.0370Å	[53]

In another series of experiments, the influence of cooling rate was studied in Sn-5Ag using the same parameters but cooling at one of five rates: 0.05, 0.2, 1.2, 5 and 20 K/min (8.3×10^{-4}, 3.3×10^{-3}, 2.0×10^{-2}, 8.3×10^{-2} and 3.3×10^{-1} K/s).

The liquidus temperature of Ag_3Sn in Sn-5Ag was measured by cyclic DSC using a method similar to that in previous studies [35,46-48]. The system was heated at 1.2 K/min to a temperature where a mixture of liquid and Ag_3Sn is known to exist (242 °C), and was then isothermally held for 30 min. The system was then heated at 1.2 K/min to 280 °C and cooled at 5 K/min to 150 °C, ending the first cycle. The isothermal holding temperature for the subsequent cycle was set to be 2 °C higher than the previous one. The presence of an endothermic peak on heating was taken to indicate that some Ag_3Sn remained at the prior isothermal holding temperature. The absence of an endothermic peak on heating indicated all Ag_3Sn had melted at the prior isothermal holding temperature. The liquidus temperature was defined as the average of the holding temperatures either side of the transition from an endothermic peak to no endothermic peak. This gave an Ag_3Sn liquidus in Sn-5Ag of 247±1 °C. This method is overviewed in more detail in the Supplementary Information.

To explore a much higher cooling rate, some Sn-3.5Ag/Cu joints were heated to 230 °C on a hot plate, held for 10 min and then quenched in water.

2.3. Optical and electron microscopy

Samples were mounted in Struers VersoCit acrylic cold mounting resin and then ground to 4000 grit with SiC paper followed by polishing with colloidal silica on a nap cloth for 6 min.

Polarised optical microscopy was used to reveal different orientations of Ag_3Sn plates, taking advantage of the optical anisotropy of orthorhombic Ag_3Sn. For scanning electron microscopy (SEM), a Zeiss Sigma field emission gun SEM fitted with Bruker e-FlashHR electron backscatter diffraction (EBSD) detector and XFlash 6130 energy-dispersive spectrometry (EDS) detector were used. Bruker Esprit 2.2 software, combined with the Orientation Imaging Microscopy (OIM™) Data Analysis software and MTEX 4.4 Toolbox within MATLAB™9.2 (Mathworks, USA), were applied to analyse the growth habits of Ag_3Sn single crystals, the orientation relationships in twinned crystals, and the orientation relationships between Ag_3Sn and the Cu_6Sn_5 reaction layer.

The crystal structures for Ag_3Sn and Cu_6Sn_5 assumed in this study are listed in Table 1. While the Cu_6Sn_5 phase present at room temperature is likely to be superstructure ordered monoclinic η' and/or η'' [49–51], we use the high temperature parent hexagonal phase η-Cu_6Sn_5 for indexing because this phase was present during solidification. Throughout this paper, all unit cell wireframes in Figures were plotted based on the Euler angles measured by EBSD.

To study the 3D morphology of Ag_3Sn and the local geometrical features of the Cu_6Sn_5 reaction layer, β-Sn was selectively etched in a solution with 5% NaOH and 3.5% orthonitrophenol at 80 °C for approximately 6 h. Extracted crystals were collected and placed on a stub for further study by analytical SEM.

To identify the main facets, electron transparent samples were milled from extracted Ag_3Sn single crystal plates using a focused ion beam (FIB) of a TFS Helios 5 CX DualBeam FIB-SEM. The lamellae were used to

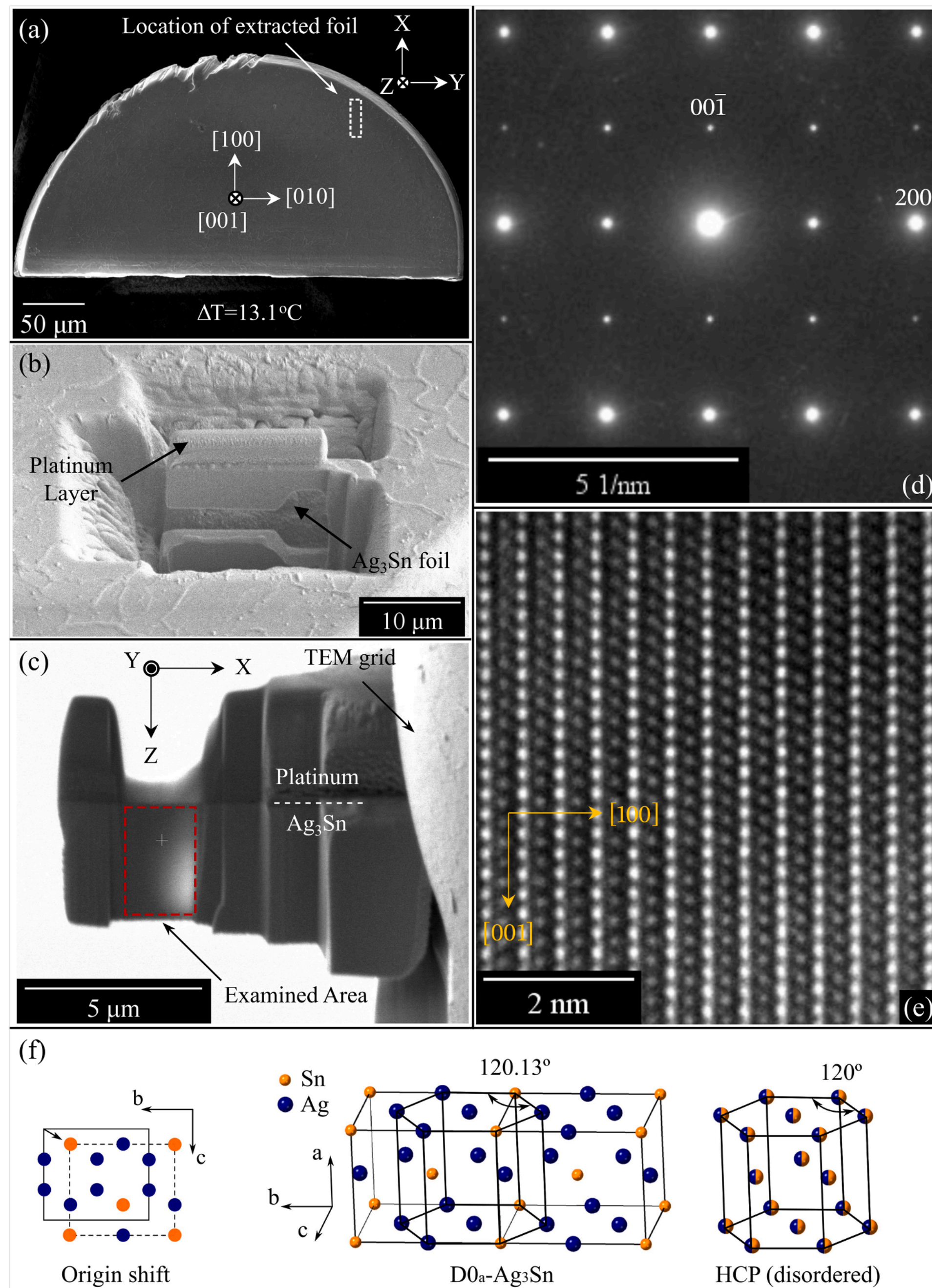

Fig. 1. (a) Ag_3Sn single crystal plate extracted from Sn-5Ag cooled at 0.05 K/min where Ag_3Sn nucleated at 13.1 °C undercooling. (b) Ag_3Sn foil milled from Ag_3Sn plate using FIB. (c) Ag_3Sn foil attached to TEM grid, where a red box highlights the examined area in TEM. (d) Selected area electron diffraction pattern (SAED) along $[0\bar{1}0]$. (e) High resolution TEM image along $[0\bar{1}0]$. (f) Orthorhombic Ag_3Sn structure compared with a hexagonal close-packed unit cell.

determine the facet orientations using selected area electron diffraction (SAED) in a TFS Talos F200i transmission electron microscope (TEM).

2.4. Real time X-ray imaging

Sn-4Ag-0.5Cu solders were rolled down to ~100 μm foils before being punched into discs with a diameter of ~500 μm. The disc foils were then placed on a ~100 μm thick Cu-OSP printed circuit board (PCB) with flux and mounted between SiO_2 glass sheets that held the sample perpendicular to the X-ray beam. A first soldering process was carried out on a hot plate before synchrotron experiments to ensure proper joining. The synchrotron experiments were conducted at BL20XU in the Spring-8 synchrotron under 1 atm pressure of nitrogen gas using the same apparatus as in Ref. [54–56]. An X-ray beam energy of 29 KeV was used. The imaging unit incorporated a phosphor screen and a CMOS camera, resulting in a field of view of 1038 μm x 1038 μm (2048 × 2048 pixels) with a resolution of 0.507 μm. The imaging exposure time was ~400 ms per frame recorded at 2 frames per second. A thermocouple was placed near the sample in the furnace to record the cooling curves and the temperatures were calibrated by the eutectic onset melting temperature. The peak temperature was 246 °C and the cooling rate was ~0.3 K/s prior to the nucleation of β-Sn.

After solidification, the synchrotron sample was soaked in acetone to remove the SiO_2 plates and the sample was then mounted in Struers VersoCit acrylic cold mounting resin, polished to an OPS finish, and studied by EBSD. The surface microstructure could then be correlated

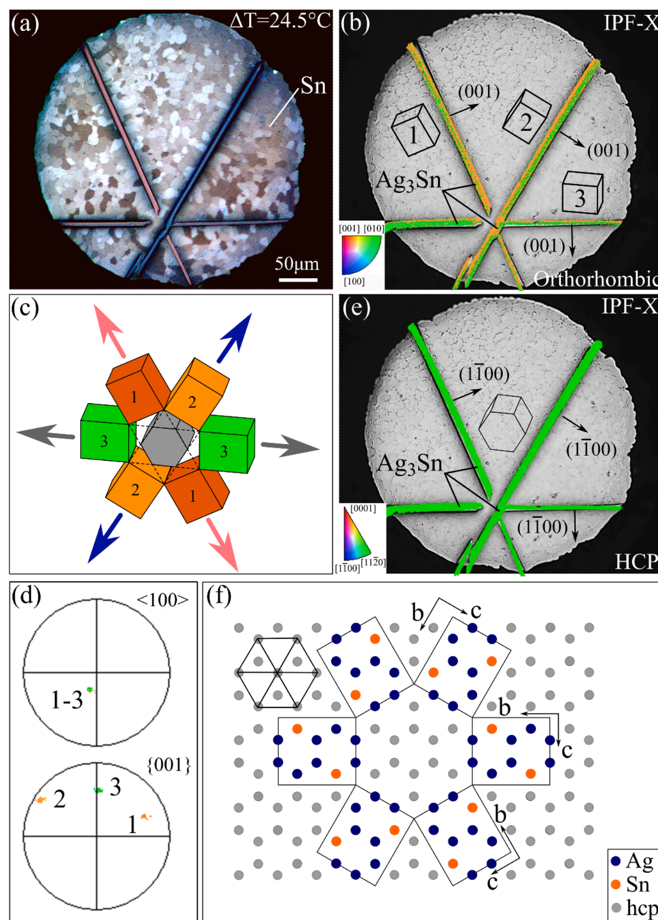

Fig. 2. Cyclic twinned Ag_3Sn in a Sn-5Ag ball with 24.5 °C undercooling cooled at 5 K/min. (a) Polarised optical microscope image of three interpenetrating Ag_3Sn plates, each having a single colour. (b) EBSD IPF-X map superimposed on the optical image with unit cell wireframes plotted next to each plate. (c) The three Ag_3Sn unit cell wireframes from (b) translated into a ring. Growth arrow colours correspond to the polarised image in (a); unit cell colours correspond to the IPF-X colouring in (b). (d) ⟨100⟩ and {001} pole figures of the three cyclic twinned orientations. (e) EBSD IPF-X map of the Ag_3Sn indexed with hexagonal unit cell. (f) Hexagonal close-packed atoms (grey) superimposed with ordered Ag (blue) and Sn (orange) atoms from the three cyclic twinned Ag_3Sn orientations.

with the projected X-ray images from the in-situ image sequence.

3. Results and discussion

3.1. Ag_3Sn in binary Sn-Ag freestanding balls

3.1.1. Crystallography of Ag_3Sn plates

Ag_3Sn commonly grew as faceted single crystal plates. As an example, Fig. 1(a) is an extracted Ag_3Sn plate from a Sn-5Ag solder ball cooled at 0.05 K/min where the nucleation undercooling for Ag_3Sn was measured to be 13.1 °C. To identify the main facet of the plate, combined FIB-TEM analysis was performed. A foil was prepared by FIB milling of the extracted plate surface in the geometry and orientation shown in Fig. 1(a) and (b), followed by Pt-deposition of the foil sample into a TEM grid (Fig. 1(c)). The TEM-SAED pattern from the thin foil sample in Fig. 1(d) was indexed with ⟨010⟩ being the zone axis. Thus, the plate is orientated as indicated by the annotated coordinate system on Fig. 1(a), and (001) is the main facet. Note that Ag_3Sn is orthorhombic where $\langle 100\rangle \neq \langle 010\rangle \neq \langle 001\rangle$. Similar FIB-TEM analysis on multiple other Ag_3Sn plates measured the same result with (001) as the main facet of the plate.

Ag_3Sn has the $D0_a$ structure type [52] which is a chemically-ordered derivative of the HCP structure with a small orthorhombic distortion [57] as shown in Fig. 1(f). The image in Fig. 1(e), which comes from the region of the SAED pattern, contains clear {100} planes which correspond to the close-packed {0001} plane in the pseudo-hexagonal structure.

SEM-based EBSD on Ag_3Sn was prone to orientation misindexing due to the hexagonal pseudo-symmetry in Fig. 1(f). For example, using Hough transform-based auto-indexing, extracted Ag_3Sn plates such as that in Fig. 1(a) auto-indexed as three orientations implying a facet of (001), (021) or (02$\bar{1}$). However, FIB-TEM showed that the main facet was always (001) which easily allowed the correct orientation to be selected from the three candidate orientations in EBSD.

3.1.2. Cyclic twinned Ag_3Sn crystals

Another common growth morphology was cyclic twinned Ag_3Sn plates. Fig. 2 shows a typical example in a Sn-5Ag solder ball cooled at 1.2 K/min with nucleation undercooling of 24.5 °C. Three interpenetrating plates span the entire solder ball. Fig. 2(a) is a polarised optical micrograph revealing three different colours of Ag_3Sn where each plate has one colour (salmon, blue or brown), indicating that each plate corresponds to a different crystallographic orientation. Three Ag_3Sn orientations were measured by EBSD mapping but, as shown in the IPF-X map in Fig. 2(b), there is strong orientation misindexing between the three orientations in the map. However, according to the FIB-TEM analysis in Section 3.1.1, the main facet of each Ag_3Sn plate is {001} and therefore, the corresponding orientation of each plate could be assigned as plotted next to each plate in Fig. 2(b). This reveals that there is a cyclic twinning relationship between the three Ag_3Sn plates involving multiple 60° rotations about the common ⟨100⟩ direction, and the three twinned orthorhombic orientations form a combined pseudo-hexagonal symmetry, as shown in Fig. 2(c) and (d).

Further insights can be gained by reanalysing the EBSD map using the pseudo-hexagonal unit cell as shown in Fig. 2(e). From this, we see that all three plates share the same pseudo-hexagonal orientation, and the facets of all plates correspond to the {1$\bar{1}$00} planes of the pseudo-hexagonal unit cell. A similar phenomenon was reported by Mueller et al. [45], from which they concluded that all the plates originated from a common centre.

The cyclic twin can be visualised by superimposing the atoms of the three orthorhombic Ag_3Sn orientations onto a hexagonal close-packed structure, as in Fig. 2(f) forming a ring consistent with the measured orientations in Fig. 2(c). The near-perfect matching between the Ag_3Sn and HCP atomic sites in Fig. 2(f) is due to Ag_3Sn having a small orthorhombic distortion of only ~0.13° from an HCP structure. The simple arrangement in Fig. 2(f) is intended to show the symmetry of the cyclic twin and does not indicate anything about the atomic structure of the common growth centre. Potential cyclic twin formation mechanisms are discussed in Section 3.1.5 after presenting the dependence of cyclic twinning on the imposed cooling rate and the Ag_3Sn nucleation undercooling in the next sections.

3.1.3. Effect of Ag_3Sn undercooling on growth morphology

Fig. 3 overviews the role of undercooling on the growth of primary Ag_3Sn in Sn-5Ag balls with a constant imposed cooling rate of 5 K/min. Results from seven balls are presented with Ag_3Sn nucleation undercoolings ranging from ~17 – 68 °C. The figure is arranged such that the Ag_3Sn nucleation undercooling becomes deeper by ~10 °C in each row from Fig. 3(a) to (g) (except Fig. 3(f)). For each Sn-5Ag ball, the DSC cooling curve is plotted with the measured Ag_3Sn liquidus temperature highlighted and the Ag_3Sn undercooling marked. The SEM image, polarised optical microscope image and EBSD IPF-Z map of the primary Ag_3Sn are also shown. The orthorhombic and pseudo-HCP unit cells from Fig. 1(f) are plotted on the IPF-Z maps to show the relationship between the measured orientations. As can be seen, Ag_3Sn grew as a

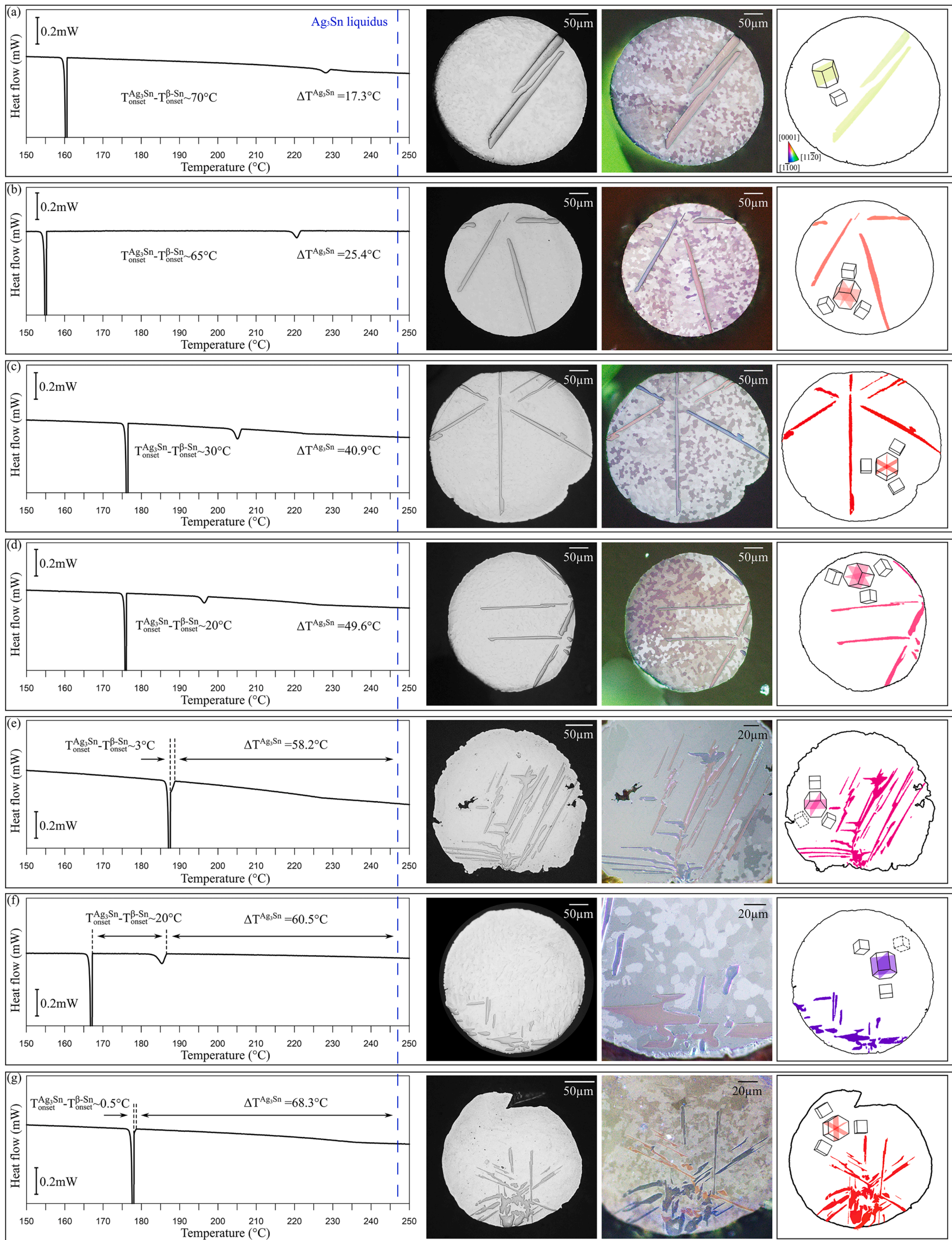

Fig. 3. Microstructures of Ag_3Sn with different nucleation undercooling in Sn-5Ag cooled at 5 K/min. DSC cooling traces highlighting the Ag_3Sn liquidus temperature (blue dashed line) and Ag_3Sn undercooling. Polarised optical images showing Ag_3Sn regions with the same orientation. EBSD IPF-Z maps plotted after indexing with an HCP structure. The hexagonal and orthorhombic unit cell wireframes are plotted from Euler angles with the hexagonal $\{1\bar{1}00\}$ planes highlighted.

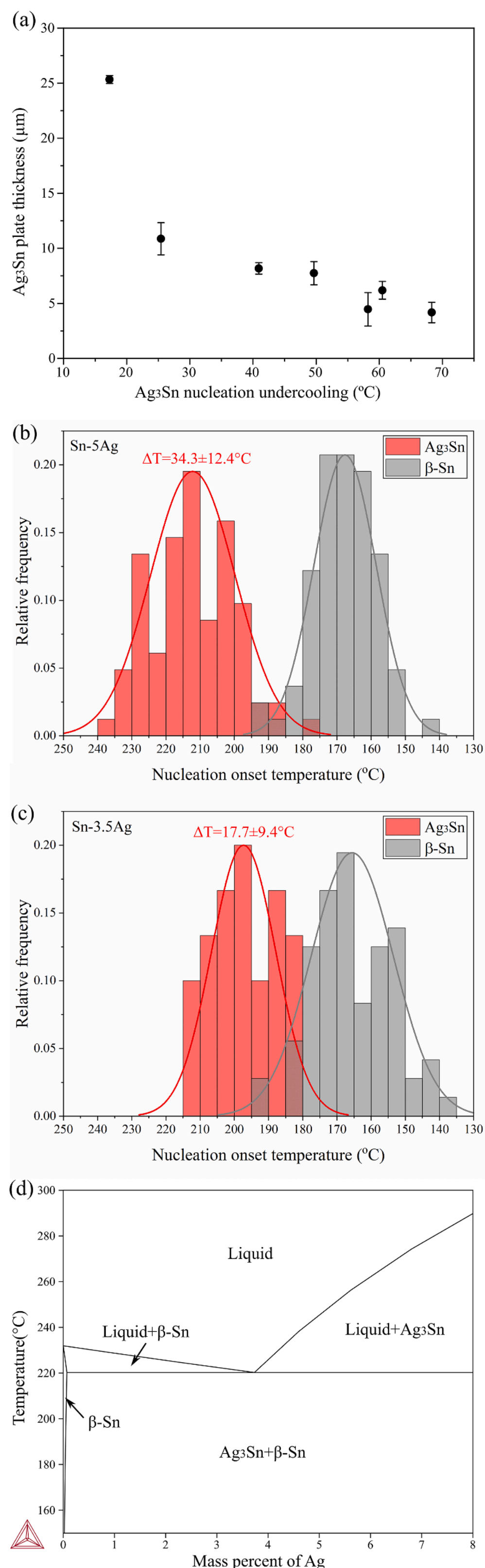

Fig. 4. (a) Ag_3Sn plate thickness versus undercooling measured from Fig. 3 using the orientation from EBSD to account for sectioning effects. (b)-(c) Histogram of nucleation onset temperature for Ag_3Sn (red) and β-Sn (grey) in 82 Sn-5Ag (b) and 30 Sn-3.5Ag (c) solder balls with fitted normal distribution curves and mean Ag_3Sn nucleation undercooling and standard deviations. Both compositions were cooled at 5 K/min. (d) Sn-Ag phase diagram at the Sn-rich side [61].

single crystal plate at the smallest undercoolings (<20 °C). With deepening undercooling to ~25 °C, three plates formed each with a different single colour in polarised light imaging and all with the same pseudo−HCP orientation in EBSD mapping, with the three orthorhombic orientations related by multiple 60° rotations around ⟨100⟩ similar to Fig. 2. Thus, the three plates grew from a common origin. Note that the examples in Fig. 3(b) and Fig. 2 are at a similar Ag_3Sn undercooling and have a similar cyclic twinned Ag_3Sn plate microstructure but the nucleation point is further from the cross-section in Fig. 3(b) than in Fig. 2, which will be the general case for a random cross-section.

When the undercooling exceeded ~40 °C, there were still three colours observed in polarised light imaging but the Ag_3Sn plates also branched during growth and formed parallel plates. Such branching became more frequent at deeper undercooling. For example, there is one parallel plate in Fig. 3(c) and (d), and multiple parallel plates in Fig. 3 (e)-(g).

When examining Fig. 3, note that parallel plates always have the same single colour in polarised light imaging (and nonparallel plates always have a different colour), all plates are consistent with {001} facets, and all plates within one ball share the same pseudo-HCP orientation indicating a single Ag_3Sn nucleation event per sample. Combining all parts of Fig. 3 we can see how the undercooling, which determines the growth velocity, affects crystal growth: (i) at the smallest undercoolings Ag_3Sn grew as single crystal plates; (ii) as the undercooling deepened Ag_3Sn grew as cyclic twinned plates where the twinning occurred only at the start of growth; (iii) at deeper undercooling, the cyclic twinned plates additionally branched during growth by twin-mediated branching resulting in multiple parallel plates; and (iv) the extent of twin-mediated branching increased as the undercooling became deeper resulting in more complicated and irregular shapes.

At deeper undercoolings, the nucleation of β-Sn started to affect the growth of Ag_3Sn, as shown in Fig. 3(e)-(g). For Fig. 3(e) and (g), there is a small temperature (and time) interval between the nucleation of Ag_3Sn and β-Sn, allowing the Ag_3Sn to retain its growth shape from rapid growth by being 'quenched' by rapid β-Sn growth. For example, from the cooling curve in Fig. 3(e) the undercooling for primary Ag_3Sn is 58.20 °C, and β-Sn formed soon (~3 °C) after Ag_3Sn nucleation. In contrast, Fig. 3(f) shows a sample with similar Ag_3Sn undercooling (60.50 °C) but different β-Sn nucleation temperature which is ~20 °C below Ag_3Sn nucleation allowing more time for Ag_3Sn growth and coarsening.

The Ag_3Sn plate thickness was measured for the plates in Fig. 3(a)-(g) correcting the 2D measurements by accounting for the tilt angle between the (001) plate normal and the sectioning plane using the Euler angles obtained from EBSD. The Ag_3Sn plate thickness is plotted versus undercooling in Fig. 4(a). The plate thickness decreases as the undercooling becomes deeper and there is also an effect of the temperature interval between the nucleation of Ag_3Sn and β-Sn (as indicated in Fig. 3) which determines the growth time for Ag_3Sn. In general, the plate thickness decreases with decreasing temperature interval and, comparing the primary Ag_3Sn crystals with similar undercooling but significantly different growth time in Fig. 3(e) and (f), it is clear that Ag_3Sn plates have the tendency to coarsen during growth.

The competition between β-Sn nucleation and primary Ag_3Sn nucleation is overviewed in Fig. 4(b)-(c) as histograms of the measured nucleation onset temperature of Ag_3Sn and β-Sn in Sn-5Ag and Sn-3.5Ag solder balls. The Sn-Ag binary phase diagram at the Sn-rich side from Thermo-Calc TCSLD4.1 is given in Fig. 4(d). For Sn-5Ag the measured nucleation temperatures for Ag_3Sn and β-Sn both follow Gaussian distributions due to the stochastic nature of the nucleation event, and the two distributions have only a small fraction of their tails overlapping indicating that, in most Sn-5Ag solder balls, the chance of primary Ag_3Sn nucleation being interrupted by β-Sn nucleation is fairly small. However, for Sn-3.5Ag as the Ag_3Sn liquidus temperature decreases to 215 °C, the distribution for Ag_3Sn shifts to lower temperature and starts to have a large fraction overlapping with β-Sn such that once a Sn-3.5Ag ball

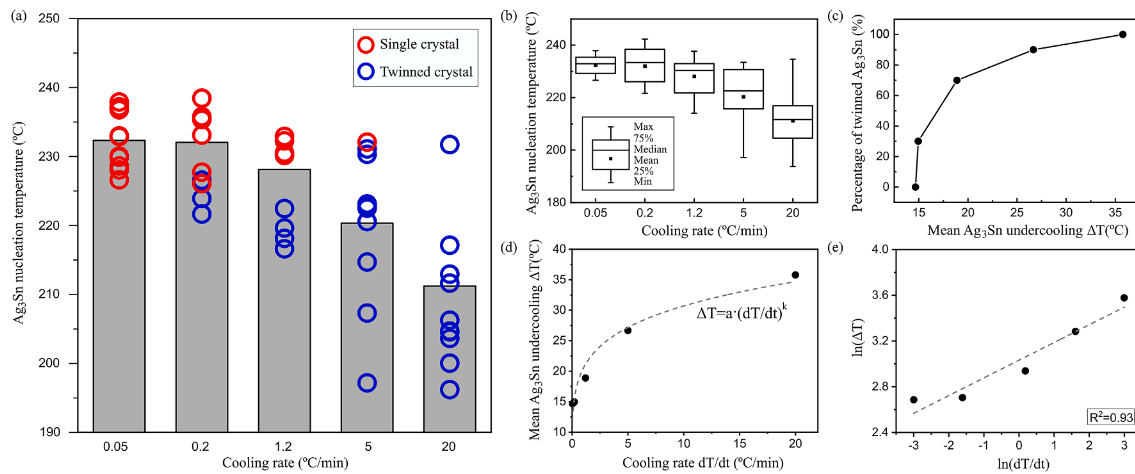

Fig. 5. (a) Ag_3Sn nucleation in Sn-5Ag at five cooling rates. Grey bars are mean temperature superimposed with the nucleation temperature of Ag_3Sn from 10 individual samples in red (single crystal) and blue (twinned crystal) circles. (b) Box plot of the measured Ag_3Sn nucleation onset temperature at different cooling rates. (c) Percentage of twinned Ag_3Sn versus the mean undercooling from different cooling rates. (d)-(e) The relationship between mean undercooling for Ag_3Sn nucleation and cooling rate. (a = 18.6, k = 0.17 for the fitting curve).

enters the overlapping region, the nucleation of β-Sn may happen first and prevent primary Ag_3Sn from forming. This competition between the nucleation of Ag_3Sn and β-Sn also changes the mean value of nucleation undercooling measured for primary Ag_3Sn: for Sn-5Ag the measured undercooling for Ag_3Sn is 34.3 ± 12.4 °C, and for Sn-3.5Ag it is almost halved: 17.7 ± 9.4 °C, indicating that it is more difficult to achieve deep Ag_3Sn undercooling in Sn-3.5Ag due to the interruption by β-Sn nucleation.

In this study, the nucleation of primary Ag_3Sn in freestanding solder balls was measured to be stochastic and relatively deep (Fig. 4), which indicates nucleation difficulties for primary Ag_3Sn similar to those for β-Sn. This finding is significantly different to statements in the literature that the nucleation and ensuing growth of Ag_3Sn occurs with minimal undercooling [11,12,34,37,38,41,58-60]. One reason for this discrepancy is the different sample mass used in past work. For example, in the DTA study of Moon et al. [35] their samples were much larger (2 g) than solder balls and their primary Ag_3Sn exhibited undercooling ≤5 °C.

3.1.4. Effects of cooling rate on growth morphology

Fig. 5 is a summary of the relationship between cooling rate, nucleation undercooling and twinning frequency in Sn-5Ag. The mean nucleation temperature for Ag_3Sn from 10 Sn-5Ag balls for each cooling rate is plotted in grey in Fig. 5(a). For each cooling rate, 10 samples with a range of undercooling were examined and the results are indicated by the red (single crystal) and blue (cyclic twinned) circles with respect to their Ag_3Sn nucleation onset temperature. At the lowest cooling rate (0.05 K/min), all Ag_3Sn were single crystals. With increasing cooling rate (0.2, 1.2 and 5 K/min), more Ag_3Sn grew as twinned crystals which tended to form at lower temperature compared to the single crystals, i.e. the twinned crystals formed at deeper undercooling. At the highest cooling rate (20 K/min), all Ag_3Sn formed as twinned crystals. In order to visualise the nucleation temperature data, Fig. 5(b) is a box plot for all the nucleation onset temperatures collected from the five cooling rates. We can see that, although for each cooling rate there is a wide range between the minimum and maximum value, the median and the mean value from each group give a clear trend that, with increasing cooling rate, the onset temperature for Ag_3Sn nucleation decreases. The mean undercooling at different cooling rates was calculated from Fig. 5(b) with the liquidus temperature for Ag_3Sn in Sn-5Ag measured as 247 °C with the cyclic DSC experiment. Fig. 5(c) quantifies the relationship between the twinning frequency and undercooling: the deeper the undercooling, the more likely that Ag_3Sn grows as a twinned crystal.

Furthermore, in Fig. 5(b) the range of Ag_3Sn nucleation temperatures at each cooling rate indicates that the nucleation of Ag_3Sn in each small (~500 µm diameter) ball is independent and stochastic, but the whole group of statistical data in Fig. 5(b) reveals a clear trend between the nucleation undercooling and cooling rate: the higher the cooling rate, the deeper the undercooling that is reached in the melt. The relationship between the measured undercooling for Ag_3Sn and cooling rate are plotted in Fig. 5(d) and (e): the mean nucleation undercooling increases with cooling rate with a near-linear increase of ln(ΔT) with respect to ln (dT/dt), as shown with the logarithmic coordinates in Fig. 5(e). A similar relationship has also been reported in other systems [62–64].

3.1.5. Origins of cyclic twinning in Ag_3Sn

From the previous sections, we see that cyclic twinning depends mostly on the undercooling at which Ag_3Sn nucleates, with deeper undercoolings promoting cyclic twin formation. We next consider possible mechanisms leading to cyclic twinned Ag_3Sn.

Cyclic twins in Ag_3Sn are three interpenetrating plates that emanate from a common centre (Fig. 2). Thus, cyclic twinning is expected to originate during the nucleation process and/or the very early stages of growth in the undercooled melt. Indeed, towards the end of this paper, we present real-time synchrotron imaging of Ag_3Sn cyclic twin growth in a solder joint on a copper substrate that directly proves that the cyclic twin grows from a common point from the earliest time that the crystal could be resolved.

From Fig. 1(f), we note that the atomic positions in the Ag_3Sn crystal structure are almost identical to the HCP structure and that the lower symmetry orthorhombic structure arises mostly from chemical order in the crystal structure. Thus, one possibility is that cyclic twinning in Ag_3Sn emerges from chemical disorder at the start of solidification. There are various ways that this might happen. One is that the nucleus structure may be chemically disordered or have imperfect chemical ordering, raising the symmetry to hexagonal. Another way is that disorder trapping may occur in the early stages of growth if the initial solid-liquid interface velocity is sufficiently high that equilibrium chemical-ordering is not achieved when atoms join the advancing interface at high undercooling [65,66]. This too could result in initial growth with metastable hexagonal symmetry. It may not be necessary to have full disorder trapping, a high density of growth defects may be enough to give the first nanoscale solid hexagonal rather than orthorhombic symmetry. The subsequent growth of the equilibrium orthorhombic Ag_3Sn structure from an HCP-like centre could occur in various ways. For example, the hexagonal structure could transform into orthorhombic Ag_3Sn by a disorder-order type reaction, or orthorhombic

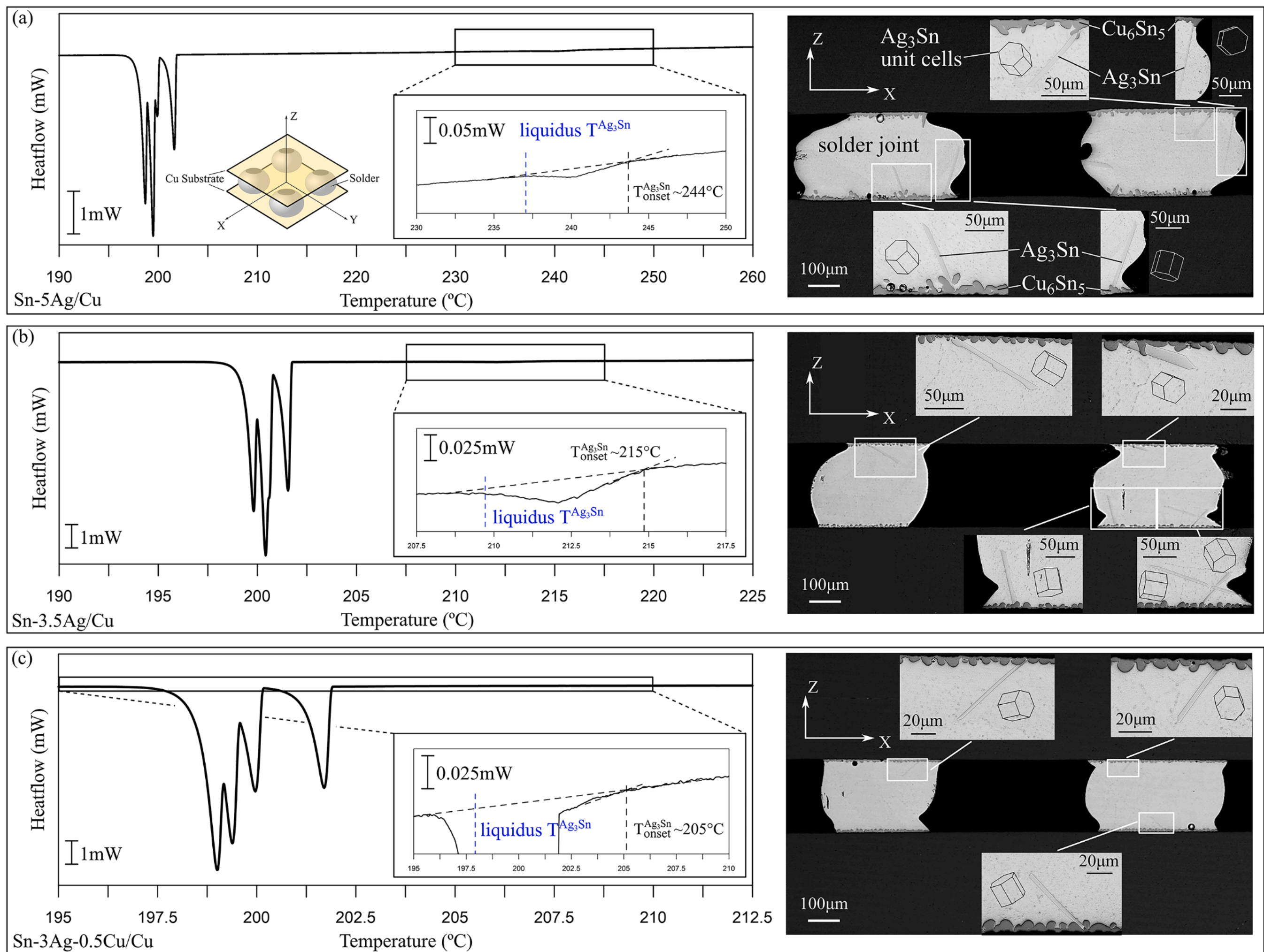

Fig. 6. DSC cooling curves and microstructures of 2 × 2 solder joint arrays with Cu substrates: (a) Sn-5Ag, (b) Sn-3.5Ag and (c) Sn-3Ag-0.5Cu. The calculated Ag_3Sn liquidus temperature is highlighted in blue dashed lines with nucleation onset temperature indicated by the extrapolation method. Orientations of the Ag_3Sn plates were plotted using hexagonal unit cell wireframes measured by EBSD.

Ag_3Sn could nucleate on the HCP centre and grow off epitaxially. Both would result in the three orientations of Ag_3Sn growing from a common centre, each one a variant of the following orientation relationship (OR) with respect to a single HCP orientation. To obtain evidence for or against these ideas, future research could study the local structure and chemical ordering at the centre of Ag_3Sn cyclic twins with atomic resolution characterisation techniques.

$$\{001\}_{Ag3Sn} \parallel \{10\bar{1}0\}_{HCP} \ \& \ \langle 100\rangle_{Ag3Sn} \parallel \langle 0001\rangle_{HCP}$$

A second possibility is that cyclic twinning may be related to growth twinning in the early stages of growth without chemical disorder at the start of solidification. Our results in Fig. 3(d-g) show that growth twinning occurred away from the nucleation point when the bulk undercooling reached ~50 °C, resulting in complex-shaped branched crystals. It is feasible that similar growth twinning could occur close to the nucleation point at smaller undercooling generating three orientations in the very early stages of solidification. The driving force for growth twinning seems to be related to the preferred growth directions of Ag_3Sn. This orthorhombic phase is constrained by crystal symmetry to grow as a {001} plate (Fig. 1(a)-(e)) which produces quasi-2D growth. Multiple growth twinning in the very early stages of solidification would create another two orientations and allow the twinned crystal to grow more effectively in 3D when there is a high driving force (undercooling) for growth. Presumably, this is also the origin of twin-mediated branching during growth far from the nucleation point that leads to the complex branched growth shapes at deeper undercooling in Fig. 3 (e)-(g).

It is instructive to compare our findings with previous work on cyclic twinning in other phases. Ag_3Sn has similarities to cyclic twinning in other low symmetry intermetallics with a close structural relationship to a higher symmetry crystal structure, and that form during solidification as a primary phase. In these cases, the cyclic twins usually contain all variants of the orientation relationship with the higher symmetry structure. For example, cyclic twins in monoclinic $Al_{13}Fe_4$ contain ten orientations each rotated ~36° around a common ⟨010⟩ and are the ten variants of the orientation relationship with a decagonal quasicrystal to which $Al_{13}Fe_4$ is an approximant [67–69]. In another example, cyclic twins in rhombohedral Al_8Mn_5 contain four orientations each rotated ~90° around the three common $< 1\bar{1}02 >$ and are the four variants of the orientation relationship with a higher symmetry cubic gamma brass (Cu_5Zn_8) [70]. In Ag_3Sn, the cyclic twin contains three orientations that are the three variants of the orientation relationship to the higher symmetry HCP structure. All could form by mechanisms similar to those outlined above although further work is required to explore if the detailed mechanisms are the same in all these cases. It is clear that cyclic twinning is a common feature of solidification when an intermetallic compound differs from a higher symmetry crystal structure only by a small distortion and different chemical ordering (e.g. Fig. 1(f) in the case

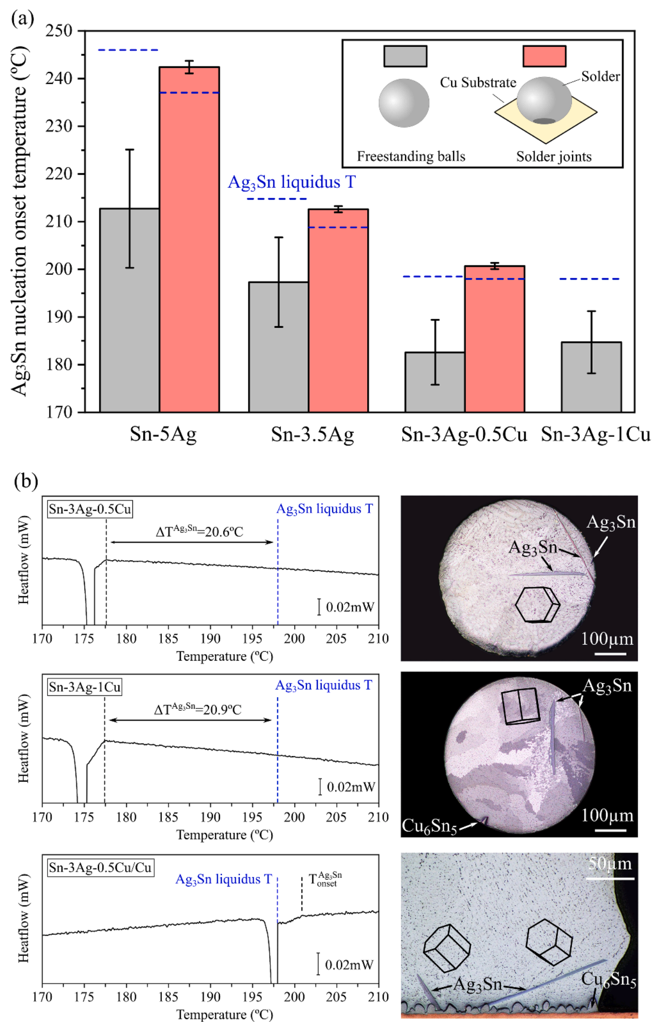

Fig. 7. (a) Mean and standard deviation nucleation onset temperature for Ag_3Sn in Sn-5Ag, Sn-3.5Ag, Sn-3Ag-0.5Ag and Sn-3Ag-1Cu freestanding solder balls (grey) and corresponding joints with Cu substrates (red). The calculated liquidus temperature is highlighted in blue dashed lines. (b) Cooling curves and microstructures for one Sn-3Ag-0.5Cu, Sn-3Ag-1Cu and Sn-3Ag-0.5Cu/Cu samples. Liquidus temperature and undercooling are marked. Polarised optical images superimposed with the orientations of Ag_3Sn plates plotted in hexagonal unit cell wireframes measured by EBSD.

of Ag_3Sn).

Another important example for electronic soldering is the cyclic twinning of tetragonal β-Sn during solidification of ball grid array solder joints [71–75]. This involves three orientations related by ~60° rotations around a common ⟨100⟩ axis [74], giving the cyclic twin pseudo-hexagonal character. Similar to Ag_3Sn, cyclic twinning in β-Sn is promoted by deeper nucleation undercooling [71]. Lehman et al. [74] proposed that cyclic twinning in β-Sn starts at the nucleation stage and presented a pseudo/metastable hexagonal nucleus structure with a Cu or Ag atom at its centre. This nucleus structure is simpler and requires less atomic organisation than the stable β-Sn structure, which is analogous to a simpler chemically-disordered HCP nucleus for Ag_3Sn. However, Ag_3Sn is a simpler case since orthorhombic Ag_3Sn differs from the higher symmetry HCP structure only by chemical ordering (Fig. 1(f)).

3.2. Ag_3Sn in Sn-Ag-Cu alloys and joints on copper substrates

The effects of soldering to a Cu substrate are presented in Fig. 6 using Sn-5Ag/Cu, Sn-3.5Ag/Cu and Sn-3Ag-0.5Cu/Cu joints as examples. For each composition, a 2 × 2 array of joints was used, similar to the inset sketch in Fig. 6(a), and reflowed in the DSC by holding for 10 min at the peak temperature (280 °C for Sn-5Ag/Cu, and 230 °C for Sn-3.5Ag/Cu and Sn-3Ag-0.5Cu/Cu) before cooling at 5 K/min in the DSC. In each case four peaks associated with β-Sn nucleation and growth can be identified in the DSC traces while the four primary Ag_3Sn peaks are smeared into one broad peak highlighted in the black boxes in the enlarged insets. Examination of the microstructures in Fig. 6 reveals that all Ag_3Sn grew as simple plates similar to Fig. 1(a) and 3(a), and there were commonly multiple plates in the cross-section that all grew from the Cu_6Sn_5 reaction layer, either the top or bottom layer or both. EBSD confirmed that all these plates are independent and correspond to different pseudo-HCP orientations, as shown in the unit cell wireframes plotted next to the plates, indicating multiple Ag_3Sn nucleation events in these joints. From Fig. 6, we can conclude that soldering to a Cu substrate in a DSC caused multiple Ag_3Sn nucleation events, simple Ag_3Sn plates without twinning, and a much narrower range of Ag_3Sn nucleation temperatures than in freestanding Sn-Ag balls in Fig. 3 and 4.

To understand how soldering to a Cu substrate catalyses Ag_3Sn nucleation compared with freestanding Sn-Ag balls (Fig. 6 versus Figs. 3 and 4), the relative importance of Cu solute, primary Cu_6Sn_5 crystals and the Cu_6Sn_5 layer are considered next by comparing freestanding balls and joints of Sn-5Ag, Sn-3.5Ag, Sn-3Ag-0.5Cu and Sn-3Ag-1Cu (wt.%). Note that Sn-3Ag-1Cu is hypereutectic with respect to the Cu_6Sn_5 liquidus and primary Cu_6Sn_5 forms before the Ag_3Sn liquidus temperature is reached.

Fig. 7(a) summarises all the measured nucleation onset temperatures for freestanding balls (grey) and Cu-substrate joints (red), together with their corresponding liquidus temperatures (blue dashed lines) for primary Ag_3Sn.

For freestanding balls in Fig. 7(a), Sn-5Ag had a deeper mean Ag_3Sn undercooling than the other three compositions because there is less interruption from β-Sn nucleation as discussed in Section 3.1.3. Sn-3.5Ag and Sn-3Ag-0.5Cu freestanding balls had similar mean Ag_3Sn nucleation undercooling (i.e. the temperature interval between the blue dashed line and the grey bar in Fig. 7(a)) and standard deviation, indicating that Cu solute in the liquid does not significantly affect the Ag_3Sn nucleation undercooling. Similarly, Sn-3Ag-0.5Cu and Sn-3Ag-1Cu freestanding balls had similar mean nucleation undercooling and deviation range, indicating that the presence of Cu_6Sn_5 primary crystals does not significantly affect the Ag_3Sn nucleation undercooling.

For solder joints with Cu substrates, the Ag_3Sn nucleation onset temperature is significantly higher than for the corresponding solder ball compositions with much narrower variation range and, similar to Fig. 6, all joints nucleated above their calculated Ag_3Sn liquidus temperature.

Three specific examples are shown in Fig. 7(b) to further illustrate these points. The first two are freestanding balls of Sn-3Ag-0.5Cu and Sn-3Ag-1Cu where the Ag_3Sn nucleated at similar undercooling and β-Sn nucleation occurred at 1~2 °C below. The Ag_3Sn plates have different colours under polarised optical microscopy indicating multiple Ag_3Sn (orthorhombic) orientations and EBSD showed these to have one pseudo-HCP orientation that is plotted as a wireframe, indicating a single Ag_3Sn nucleation event in each ball. In Sn-3Ag-1Cu, primary Cu_6Sn_5 is also present as labelled but it is located far from the Ag_3Sn and no simple orientation relationship was measured between primary Cu_6Sn_5 and Ag_3Sn in this or any other sample investigated, further showing that primary Cu_6Sn_5 did not significantly affect the nucleation of primary Ag_3Sn. The third example shows a Sn-3Ag-0.5Cu/Cu joint with multiple (two) independent Ag_3Sn plates and an Ag_3Sn nucleation onset temperature that is significantly higher than in the freestanding solder balls.

From Fig. 7, it can be concluded that solder joints on Cu substrates resulted in multiple Ag_3Sn nucleation events (Figs. 6 and 7(b)) and nucleation onset temperatures that were significantly higher than their corresponding solder balls and with much narrower variation range (Fig. 7(a)). This contrasts with Cu solute and the presence of primary

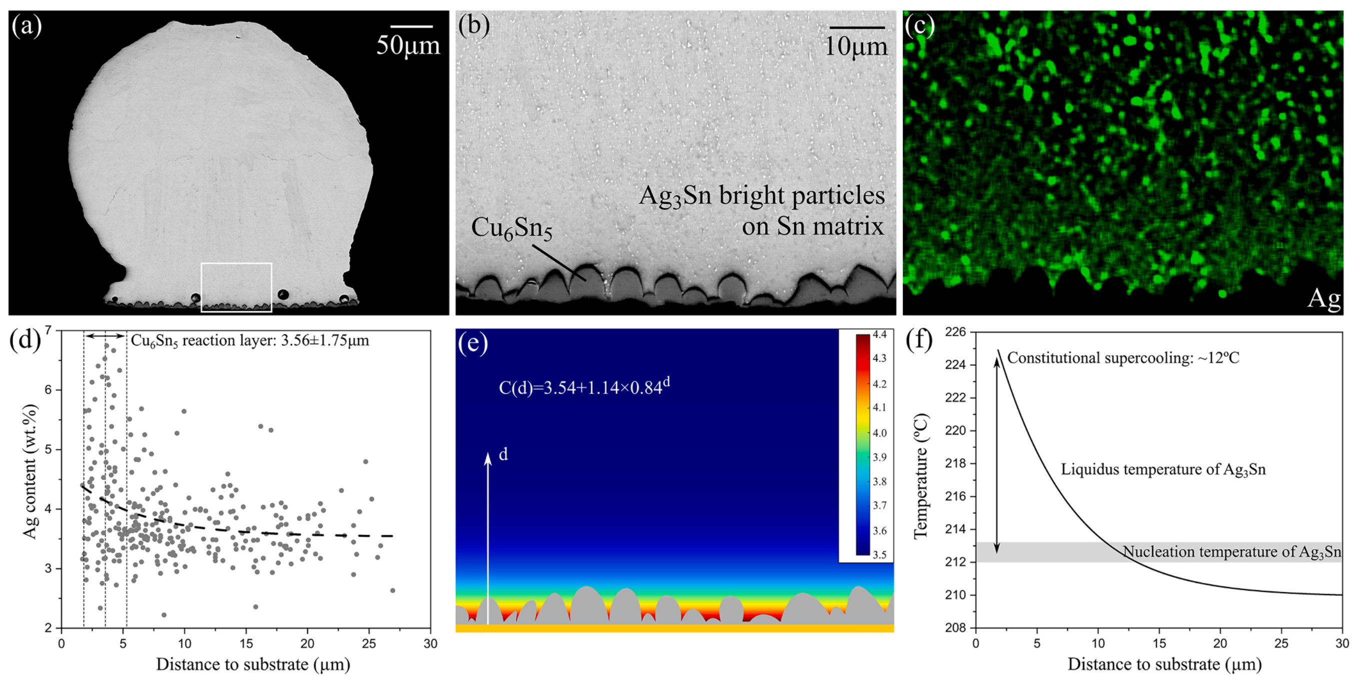

Fig. 8. (a) The microstructure of a quenched Sn-3.5Ag/Cu joint. (b) Enlarged view of the white box area in (a). (c) The EDX Ag map of the same area as (b). (d) Ag content from multiple EDX point analysis versus measured distance to the Cu substrate. The Ag distribution is fitted with the black dashed line. The thickness of Cu_6Sn_5 is plotted with vertical grey dotted lines. (e) A contour plot showing the change of Ag content near the Cu_6Sn_5 reaction layer calculated from the black dashed line in (d). The function of the fitted line is also marked. (f) The change of Ag_3Sn liquidus temperature with distance from the Cu substrate. The measured Ag_3Sn nucleation temperature range from Fig. 7 is highlighted in grey and the constitutional supercooling is highlighted close to the Cu_6Sn_5 reaction layer.

Cu_6Sn_5 crystals which had little effect on Ag_3Sn nucleation and shows that it is the Cu_6Sn_5 reaction layer that promotes the nucleation of Ag_3Sn.

To assess the Ag_3Sn nucleation undercooling in joints, we need to consider the change in liquid composition due to copper substrate dissolution. The liquidus temperature for each composition was calculated using the Thermo-Calc TCSLD4.1 database assuming that Cu solute is fully saturated in the melt at the peak temperature during holding, which is reasonable as previous experiments and calculations confirmed that, for 500 μm solder balls, 10 min are enough for Cu to saturate into the melt from the substrate [76,77]. Assuming uniform saturated melts, the calculated Ag_3Sn liquidus temperature is plotted for all compositions as blue dashed lines in Figs. 6, 7(a) and 7(b). In all cases, the Ag_3Sn nucleation onset temperature is above this Ag_3Sn liquidus temperature, making the nucleation undercooling appear negative which is unphysical. This shows that the assumption of a uniform liquid composition is invalid and we need to also consider the variation in Ag content in the liquid due to the growth of Cu_6Sn_5 layer.

In order to investigate the Ag solute field in the liquid before Ag_3Sn nucleation, Sn-3.5Ag/Cu joints were heated to 230 °C, held for 10 min and then quenched in water. The cross section of such a solder joint is shown in Fig. 8(a) where no primary Ag_3Sn plates formed. The enlarged BSE image in Fig. 8(b) highlights the small Ag_3Sn eutectic particles in the bulk and between the scallops of the Cu_6Sn_5 reaction layer. EDX elemental mapping of the same area in Fig. 8(c) reveals a highly heterogeneous Ag composition field caused by the liquid solidifying to produce a mixture of Ag_3Sn particles containing ~73 wt.% Ag and β-Sn containing ~0.07 wt.% Ag (calculated with Ref [61].). Note in Fig. 8(c) that the EDX map implies that the top Ag_3Sn particles are much larger than they are in Fig. 8(b); for more quantitative analysis EDX point analysis is required.

To quantify the original liquid solute field, averaging of more than 300 chemical analysis points near the bottom of the solder joint was performed. The individual data points are plotted in Fig. 8(d) as composition versus distance to the Cu substrate. The average thickness of the Cu_6Sn_5 reaction layer was measured to be 3.56±1.75 μm and is highlighted with the dashed lines. The data points between these lines correspond to points located in the gaps between the Cu_6Sn_5 crystals/scallops. The large scatter in the data is due to different amounts of Ag_3Sn and β-Sn phases in the electron interaction volume at each measurement point and averaging is required to access the original liquid composition. All the data points were fitted with the thick dashed line which describes the distribution of Ag content with respect to the distance to the substrate. As can be seen, the Ag content decreases with increasing distance from the substrate and, for the area far from the substrate, the mean Ag content is close to 3.5 wt.% which is consistent with the bulk composition. The function of the fitted curve is written in Fig. 8(e), together with a contour plot of this change of Ag content and a sketch of the Cu_6Sn_5 layer from the same region and scale of Fig. 8(b). From Fig. 8(e), we see how Ag solute was rejected into the liquid during Cu_6Sn_5 layer growth and accumulated naturally in the gaps and valleys between Cu_6Sn_5 scallops due to the scallop growth shape. This rejection of Ag is consistent with there being negligible solubility for Ag in the Cu_6Sn_5 phase [35].

Combining the measured Ag profile in Fig. 8(d) and (e) with calculations of the Ag_3Sn liquidus temperature for these compositions in Thermo-Calc TCSLD4.1, the relation between the Ag_3Sn liquidus temperature and distance from the Cu substrate was obtained and is plotted in Fig. 8(f). The range of measured nucleation temperatures for Ag_3Sn in Sn-3.5Ag/Cu joints in Fig. 7(a) is also plotted on Fig. 8(f) as a grey band. We see that the only locations where Ag_3Sn could have nucleated in undercooled liquid are <~10 μm from the Cu substrate. Thus, thermodynamically, we can infer that Ag_3Sn must have nucleated on or near the Cu_6Sn_5 reaction layer in all joints on Cu substrates in Figs. 6 and 7(a) because their Ag_3Sn nucleation temperatures are all above the liquidus temperature of the bulk (far field) liquid. This is a form of constitutional supercooling (up to ~12 °C in Fig. 8(f)) with respect to the Ag_3Sn liquidus temperature due to the local accumulation of Ag solute in the liquid during diffusion ahead of the Cu_6Sn_5 layer. Nucleation of Ag_3Sn on the Cu_6Sn_5 layer is also consistent with all Ag_3Sn plates being in

contact with the Cu_6Sn_5 layer in the micrographs in Fig. 6.

Fig. 8(f) also shows that, when Ag_3Sn nucleates on/near the Cu_6Sn_5 layer in constitutionally supercooled liquid, the plate can only grow up to ~10 μm in supercooled liquid and further plate growth then depends on the rate of external heat extraction which is slow for DSC cooling at 5 K/min. This is consistent with Ag_3Sn growing as single crystal plates (without growth twinning) in all joints on Cu in Fig. 6.

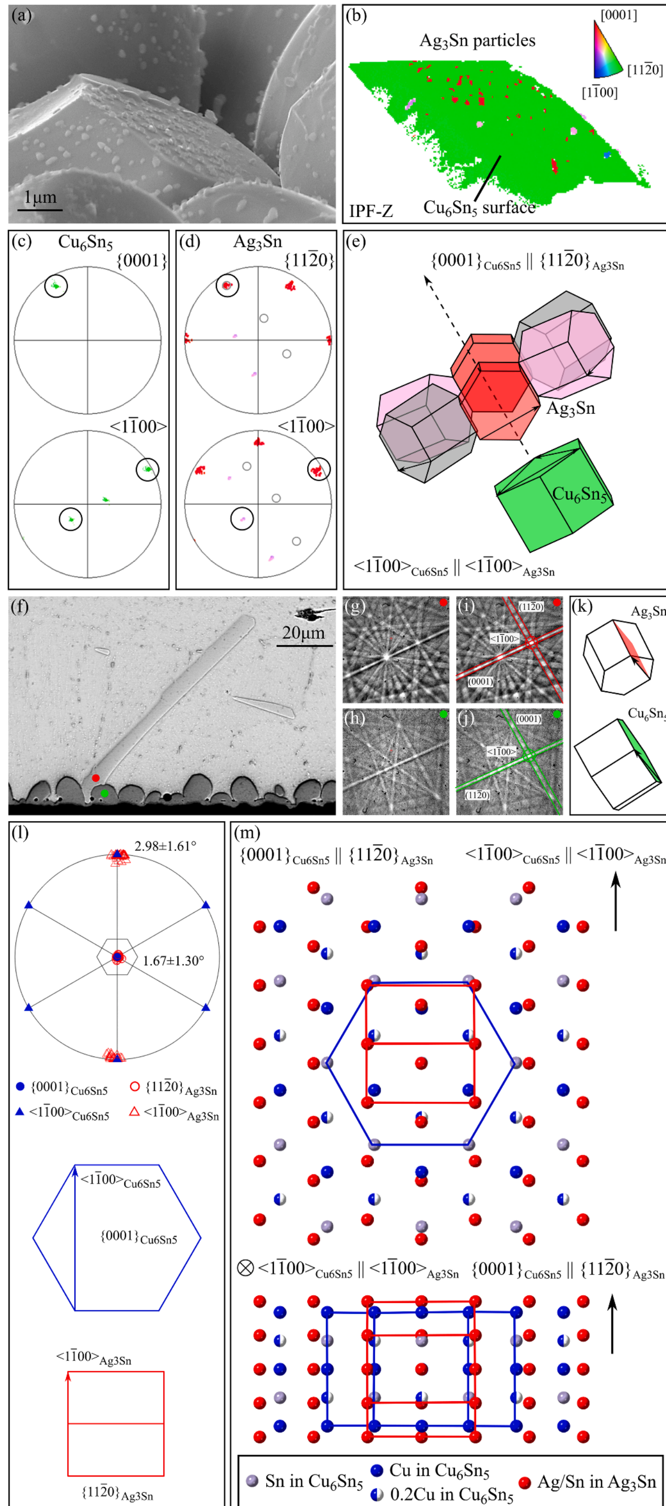

(caption on next column)

Fig. 9. (a) 70° tilt view of numerous Ag_3Sn particles on a Cu_6Sn_5 reaction layer surface after dissolving β-Sn from quenched Sn-3.5Ag/Cu joint. (b) EBSD IPF-Z map of the Cu_6Sn_5 surface in (a) with both Ag_3Sn and Cu_6Sn_5 indexed using their corresponding hexagonal structure. (c)-(d) Pole figures for the Cu_6Sn_5 and Ag_3Sn in (b) with parallel planes and directions highlighted in black circles. The $\{11\bar{2}0\}$ and $< 1\bar{1}00 >$ for the grey unit cell in (e) was also plotted with grey circles. (e) The measured orientation relationship between Ag_3Sn and Cu_6Sn_5. Three Ag_3Sn orientation variants of the OR were plotted with two of them measured (red and pink) and one calculated (grey). (f) Primary Ag_3Sn growing from Cu_6Sn_5 reaction layer with the same orientation relationship. The two crystals are marked in red and green. (g)-(h) The Kikuchi patterns from the Ag_3Sn and Cu_6Sn_5 crystals in (f). In (i)-(j) selected parallel planes and directions are indexed on the Kikuchi patterns. (k) Unit cell wireframes of the two crystals with highlighted parallel planes and directions. (l) Summary of the OR by projecting the $\{11\bar{2}0\}$ and $< 1\bar{1}00 >$ of Ag_3Sn orientations into pole figures with respect to the orientations of Cu_6Sn_5. (m) Atomic projection of Ag_3Sn and Cu_6Sn_5 on their parallel planes with unit cells highlighted.

The relatively small solute-corrected nucleation undercooling for Ag_3Sn of ~12 °C (Fig. 8(f)) with narrow variation range for Sn-3.5Ag/Cu joints (Fig. 7(a)) indicates that the nucleation site itself also has a relatively higher potency and possibly higher number density than in free-standing balls. Thus, orientation relationships (ORs) between the Cu_6Sn_5 layer and Ag_3Sn were explored. As revealed by Fig. 9(a), many small Ag_3Sn particles were sometimes attached to the Cu_6Sn_5 reaction layer surface in quenched samples, and direct EBSD on these particles revealed that many of them shared the same OR with the Cu_6Sn_5, as can be seen in Fig. 9(a)-(e). Fig. 9(a) is a 70° tilted image of a faceted Cu_6Sn_5 crystal in the reaction layer with multiple nanoscale Ag_3Sn on the surface. The EBSD IPF-Z map in Fig. 9(b) shows that there are three pseudo-HCP orientations indexed for the 49 Ag_3Sn particles: 43 Ag_3Sn in red, 5 in pink and 1 in purple. In the pole figures in Fig. 9(c) the {0001} plane of Cu_6Sn_5 is parallel to a $\{11\bar{2}0\}$ plane of the red and pink pseudo-HCP Ag_3Sn with two $< 1\bar{1}00 >$ directions of Cu_6Sn_5 parallel to one of the $< 1\bar{1}00 >$ directions in each of the red and pink pseudo-HCP Ag_3Sn respectively, as highlighted by black circles. This orientation relationship can be written as:

$$\{11\bar{2}0\}_{Ag3Sn} \| \{0001\}_{Cu6Sn5} \ \& \ \langle 1\bar{1}00\rangle_{Ag3Sn} \| \langle 1\bar{1}00\rangle_{Cu6Sn5}$$

The OR is also plotted with the unit cell wireframes in Fig. 9(e). Theoretically, there should be three Ag_3Sn pseudo-HCP orientation variants corresponding to this OR. The missing one was calculated and is plotted in grey in Fig. 9(e) with its $\{11\bar{2}0\}$ planes and $< 1\bar{1}00 >$ directions also plotted as small grey circles in pole figures in Fig. 9(d). There is only one Ag_3Sn particle (coloured in purple) at the bottom right of the surface that does not share this OR or any other simple OR with the Cu_6Sn_5 crystal.

It is then natural to ask whether large Ag_3Sn plates nucleate on the Cu_6Sn_5 layer with the same OR. Note that the Ag_3Sn plates are large and contact numerous different Cu_6Sn_5 crystals in the Cu_6Sn_5 reaction layer at the same time so we would not expect to find the nucleation OR between Ag_3Sn plates and most of the Cu_6Sn_5 scallops they contact on the reaction layer. Nevertheless, the OR was measured between some primary Ag_3Sn plates and Cu_6Sn_5 in the reaction layer. Fig. 9(f)-(k) gives an example. In Fig. 9(f), a large primary Ag_3Sn plate has the OR with a contacting Cu_6Sn_5 grain. Fig. 9(g)-(j) are the Kikuchi patterns taken from the red and green points in Fig. 9(f) with selected parallel planes and directions indexed. Since the (001) facet of Ag_3Sn can be inferred from Fig. 9(f), the correct orthorhombic orientation can be deduced from the pseudo-HCP orientation as discussed with Figs. 1 and 2. The unit cell wireframes of the two orientations are plotted in Fig. 9(k) with the parallel planes and directions highlighted. The OR can be written in terms of orthorhombic Ag_3Sn:

$$\{010\}_{Ag3Sn} \| \{0001\}_{Cu6Sn5} \ \& \langle 001\rangle_{Ag3Sn} \| \langle 1\bar{1}00\rangle_{Cu6Sn5}$$

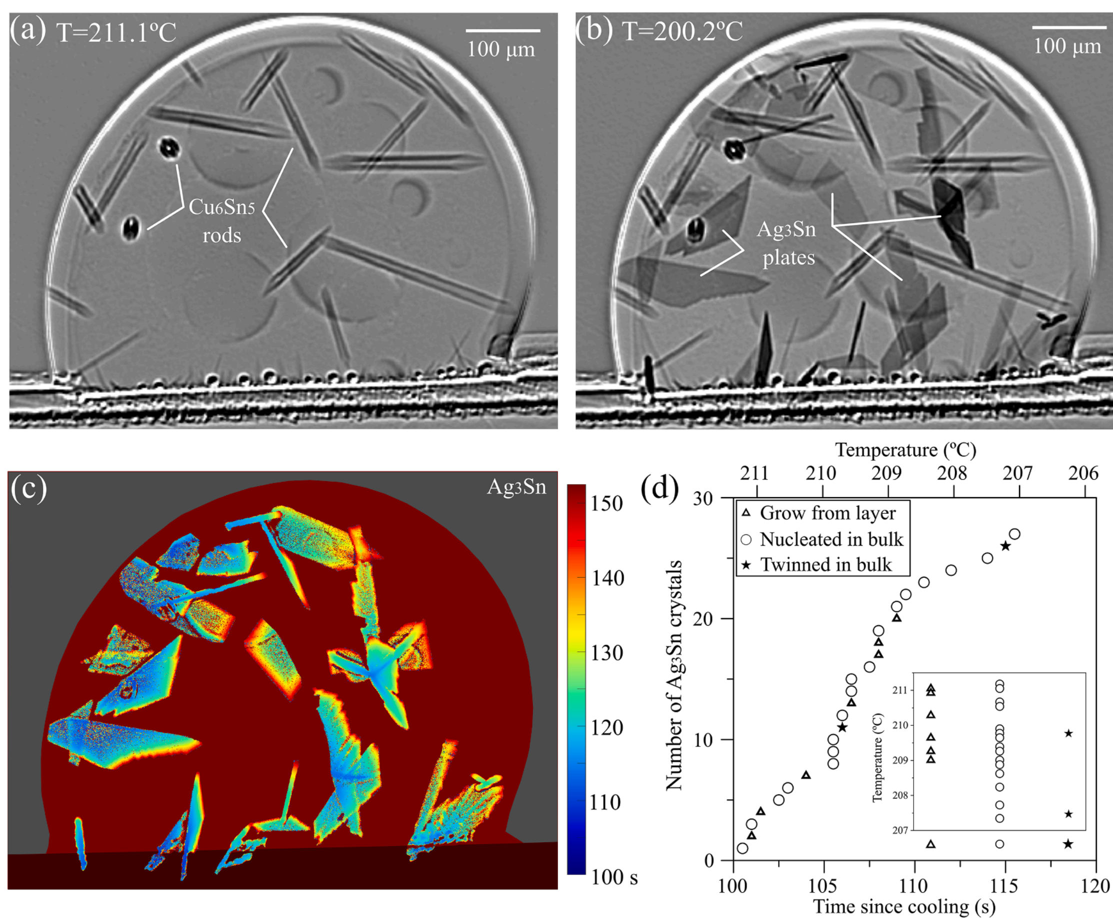

Fig. 10. Synchrotron radiography of Ag_3Sn plate solidification in a Sn-4Ag-0.5Cu/Cu joint (a) A frame at 211 °C when only primary Cu_6Sn_5 crystals are present. (b) A frame at 200 °C after the nucleation and growth of Ag_3Sn crystals and prior to β-Sn nucleation. (c) A processed image where each Ag_3Sn pixel is coloured by its Ag_3Sn formation time in seconds. (d) Total number of Ag_3Sn crystals versus time, with an inset comparing the nucleation temperatures of different Ag_3Sn types.

To assess the reproducibility of this OR, Fig. 9(l) summarises this OR over 53 Ag_3Sn crystals (both eutectic particles and primary plates) by projecting the parallel $\{11\bar{2}0\}$ plane and $<1\bar{1}00>$ direction of pseudo-HCP Ag_3Sn into the standard pole figure of Cu_6Sn_5, with the deviation annotated for the parallel plane and direction. Furthermore, the superimposed crystal lattice of the two phases in Fig. 9(m) indicates a relatively low atomic mismatch with this orientation relationship, particularly along the parallel row $\langle 1\bar{1}00\rangle_{Ag3Sn} \| \langle 1\bar{1}00\rangle_{Cu6Sn5}$ which is the vertical direction in the upper part of Fig. 9(m). However, the match is less good along other directions and the overall match is significantly worse than potent nucleants in other systems such as $PdSn_4$ and α-$CoSn_3$ for β-Sn [78,79], TiB_2 for α-Al or Al_3Ti [80,81], and Zr for α-Mg [82,83]. Thus, it seems that Cu_6Sn_5 is not a highly potent nucleant for Ag_3Sn but is the lowest energy interface available for heterogeneous nucleation in the location where the liquid is constitutionally supercooled.

Previous work has shown that the Cu_6Sn_5 layer also catalyses the nucleation of β-Sn in solder joints [84]. It was shown by FIB-tomography that the triple points between Cu_6Sn_5 scallops have a 3D shape similar to conical cavities which are known to be catalytic to nucleation [85]. Thus, three factors probably combine to promote Ag_3Sn nucleation on Cu_6Sn_5 in the reaction layer: (i) constitutional supercooling which causes the maximum melt supercooling to exist between the scallops in the Cu_6Sn_5 layer and enable Ag_3Sn nucleation at a temperature higher than the liquidus temperature of the bulk liquid away from the layer; (ii) geometrical catalysis from the conical cavity-like shapes between Cu_6Sn_5 scallops in the reaction layer; and (iii) a relatively good atomic match between Ag_3Sn and Cu_6Sn_5 for the nucleation OR.

3.3. Synchrotron study of Ag_3Sn nucleation and growth

Fig. 10 overviews synchrotron radiography results of the nucleation and growth kinetics of primary IMCs in a Sn-4Ag-0.5Cu/Cu joint. Fig. 10 (a) is a snapshot at $T = 211.1$ °C when numerous primary Cu_6Sn_5 have formed in the liquid as hollow rods (similar to Ref. [55]) and no Ag_3Sn has yet nucleated. Note that Fig. 10(a) is a through-thickness averaged radiograph and the volume fraction of Cu_6Sn_5 is much lower than it may appear from the projected image. Fig. 10(b) is a snapshot at lower temperature of $T = 200.2$ °C when multiple Ag_3Sn plates had nucleated and grown in the bulk and near the solder-substrate. There was no evidence of Ag_3Sn nucleating on the primary Cu_6Sn_5, consistent with the results with bulk solder joints.

To visualise and quantify the growth kinetics of the Ag_3Sn plates, in Fig. 10(c), pixels containing Ag_3Sn have been coloured by the time at which they first became solid Ag_3Sn. As we can see, most Ag_3Sn are single crystals growing from a nucleation point (blue) into a faceted plate. A few Ag_3Sn share a common growth centre, indicating cyclic twinning. For example, in the centre-right of Fig. 10(c), note the dark blue three-pointed star emanating from a common centre and growing into three plates of increasingly ‘hot’ colours. Thus, similar to bulk samples earlier in this paper, Ag_3Sn grew as single crystal plates and as cyclic twinned plates in the synchrotron samples. However, there was additionally a significant difference: in bulk solder joints (e.g. Fig. 6) Ag_3Sn nucleation occurred almost exclusively on the Cu_6Sn_5 reaction layer whereas, in the thin synchrotron samples, Ag_3Sn nucleation occurred both on the Cu_6Sn_5 reaction layer and throughout the ‘bulk’. We can infer that the Ag_3Sn that appear to be in the bulk are actually

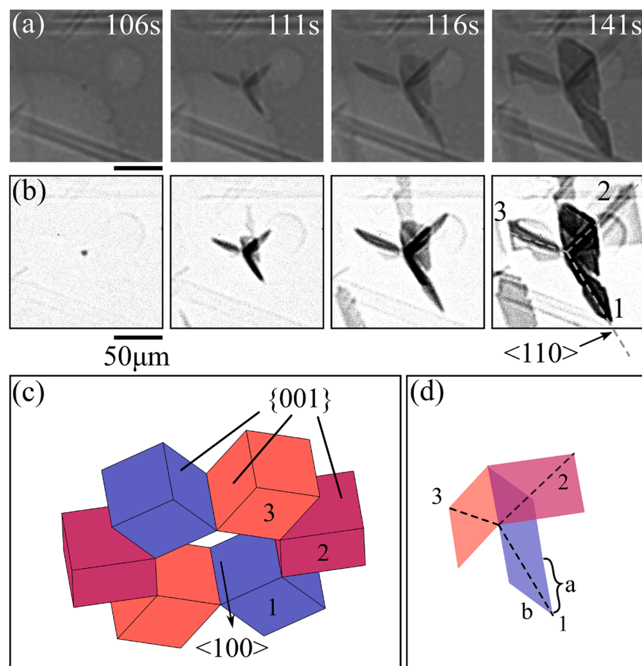

Fig. 11. (a) Synchrotron X-ray image sequence of the nucleation and growth of twinned primary Ag_3Sn in a Sn-4Ag-0.5Cu/Cu joint. (b) Images subtracted by a frame shortly before 106 s showing three plates grow from a common point. Ag_3Sn plates appear dark. (c) Cyclic Ag_3Sn unit cells showing three twinned orientations, as measured by post-mortem EBSD. (d) Three $\{001\}_{Ag3Sn}$ planes taken from the unit cells resemble the growth of actual Ag_3Sn plates in (b).

attached to (and nucleated on) the cell walls since the Ag_3Sn did not move under gravity despite being significantly denser than the liquid. Thus, the thin sample geometry affected the nucleation of Ag_3Sn, with many Ag_3Sn nucleation events forming on the walls of the cell. A further factor is that the ratio of the area of substrate to the volume of solder is much smaller in thin-sample synchrotron experiments than in solder joints, promoting Ag_3Sn nucleation away from the Cu_6Sn_5 layer. Fig. 10 (d) summarises the nucleation sequence of different types of Ag_3Sn crystals. Most of the single crystal Ag_3Sn plates growing from the reaction layer (triangles) tended to form at an earlier stage compared to the two cyclic twinned crystals (stars) observed forming in the bulk. The remaining single crystal plates nucleating on the cell walls (circles) nucleated throughout the whole time/temperature range.

Fig. 11 plots the detailed growth process of one of the cyclic twinned Ag_3Sn crystals by combined in-situ X-ray imaging and post-mortem EBSD. The in-situ radiography at different growth stages in Fig. 11(a) and (b) directly proves that the crystal comes from a common centre followed by growth into three large plates. Note that the greyscale depends on the thickness of Ag_3Sn where thicker and overlapping Ag_3Sn regions appear darker. The same three plates were identified on the surface of the specimen and EBSD was applied to measure their orientations. The measured orthorhombic unit cells from the three plates are plotted in Fig. 11(c). They are cyclic twinned with 60° to each other along a common ⟨100⟩, and form a combined hexagonal symmetry similar to Fig. 2.

Combining information from the in-situ imaging in Fig. 11(a) and (b) with the crystallographic orientations from EBSD in Fig. 11(c), the {001} planes from the three unit cells are plotted in Fig. 11(d) aligned along their common ⟨100⟩ twin axis with one of their ⟨110⟩ directions highlighted with black dashed lines emanating from a nucleation point. Note in Fig. 11(d) that the plates match well with the plate shapes in Fig. 11(a) and (b), that the three plates are rectangular (in 3D) with their edges parallel to the ⟨100⟩ and ⟨010⟩ directions consistent with Fig. 1(a), and that each plate has a tendency of thickening along the ⟨110⟩ direction emanating from the common centre. Plate 1 and 2 stopped growing due to the interruption of the nearby Cu_6Sn_5 rods while plate 3 stops growing as it impinged on the cell wall.

Even with the significant differences in the synchrotron experiments related to the sample geometry and cooling conditions (e.g. the catalytic cell walls, different area to volume effects and local temperature gradient), the key findings are consistent with the solder joints in Figs. 6 and 7. The primary Cu_6Sn_5 did not promote Ag_3Sn nucleation, while the Cu_6Sn_5 reaction layer was catalytic for Ag_3Sn nucleation such that all Ag_3Sn growing from the reaction layer were single crystal plates, while cyclic twinned crystals nucleated in the bulk at relatively deeper undercooling (Fig. 10(d)). The real-time X-ray imaging proves that cyclic twins grow from a common point, indicating that cyclic twinning of Ag_3Sn occurred either in the process of nucleation or in the very early stages of growth as discussed in Section 3.1.5.

4. Conclusions

This work has revealed the following new insights into the nucleation and growth of primary Ag_3Sn in 500μm solder balls and solder joints on copper substrates.

In freestanding Sn-Ag balls, the undercooling for Ag_3Sn nucleation is more stochastic than reported/assumed in past work, spanning the range ∼10–70 K. At the smallest undercoolings, Ag_3Sn grew as single crystal plates with {001} as the main facet. Deepening of the undercooling promoted Ag_3Sn cyclic twinning and, as the undercooling became deeper still, additional twin-mediated growth branching became increasingly common.

Cyclic twinned Ag_3Sn crystals are three interpenetrating plates linked by 60° rotations about a common ⟨100⟩ axis, forming a combined hexagonal symmetry related to the pseudo-HCP structure of Ag_3Sn. The three plates emanate from a common centre in the undercooled melt. Possible formation mechanisms include (i) the development of chemical disorder in the process of nucleation or in the very early stages of growth, which would raise the crystal symmetry from orthorhombic to hexagonal, and/or (ii) multiple growth twinning in the early stages of growth to enable the Ag_3Sn to grow in 3D in six directions rather than as a quasi-2D plate.

There is a competition between the nucleation of β-Sn and Ag_3Sn. When β-Sn nucleates first, primary Ag_3Sn is completely supressed. This can happen even for deep β-Sn undercoolings due to the stochastic nature of nucleation in both phases in freestanding balls.

Soldering to copper substrates significantly catalysed Ag_3Sn nucleation, resulting in multiple independent Ag_3Sn single crystal plates growing from the Cu_6Sn_5 reaction layer with significantly higher nucleation onset temperature and narrower variation range compared to freestanding solder balls. Cu solute and primary Cu_6Sn_5 appear to have no significant effect on the nucleation of Ag_3Sn. Instead, it is the Cu_6Sn_5 reaction layer that promotes Ag_3Sn nucleation due to (i) constitutional supercooling generated by Ag solute rejection into the liquid between the scallops of the Cu_6Sn_5 reaction layer, (ii) geometrical catalysis in the grooves between Cu_6Sn_5 scallops and (iii) heterogeneous nucleation of Ag_3Sn on Cu_6Sn_5 with the reproducible orientation relationship (OR): $\{11\bar{2}0\}_{Ag3Sn} \,||\, \{0001\}_{Cu6Sn5}$, with $< 1\bar{1}00 >_{Ag3Sn} \,||\, < 1\bar{1}00 >_{Cu6Sn5}$.

The catalysis of Ag_3Sn nucleation in solder joints results in more Ag_3Sn growing as single crystal plates and fewer growing as cyclic twinned Ag_3Sn crystals in joints compared with freestanding balls.

Declaration of Competing Interest

The authors declare that they have no known competing financial interests or personal relationships that could have appeared to influence the work reported in this paper.

Acknowledgements

This work was partially funded by the UKEPSRC Grant EP/R018863/1. The authors acknowledge use of characterization facilities within the Harvey Flower Electron Microscopy Suite, Department of Materials, Imperial College London. Synchrotron experiments were performed on BL20XU at SPring-8 in Hyogo, Japan, under grant numbers 2015A1675 and 2020A1491.

Supplementary materials

Supplementary material associated with this article can be found, in the online version, at doi:10.1016/j.actamat.2023.118831.

References

[1] C.M. Miller, I.E. Anderson, J.F. Smith, A viable tin-lead solder substitute: Sn-Ag-Cu, J. Electron. Mater. 23 (7) (1994) 595–601.
[2] N.-.C. Lee, Lead-free Soldering-Where the World is Going, Society of Manufacturing Engineers, 2000.
[3] D.A. Shnawah, M.F.M. Sabri, I.A. Badruddin, A review on thermal cycling and drop impact reliability of SAC solder joint in portable electronic products, Microelectron. Reliab. 52 (1) (2012) 90–99.
[4] P. Darbandi, et al., The effect of cooling rate on grain orientation and misorientation microstructure of SAC105 solder joints before and after impact drop tests, J. Electron. Mater. 43 (7) (2014) 2521–2529.
[5] R.J. Coyle, K. Sweatman, B. Arfaei, Thermal fatigue evaluation of Pb-free solder joints: results, lessons learned, and future trends, JOM 67 (10) (2015) 2394–2415.
[6] R. Coyle, et al., A collaborative industrial consortia program for characterizing thermal fatigue reliability of third generation Pb-free alloys, in: SMTA International, 2016.
[7] R. Coyle, et al., Enhancing thermal fatigue reliability of Pb-free solder alloys with additions of bismuth and antimony, in: SMTA International, 2020, pp. 6–19.
[8] S. Belyakov, et al., Microstructure and damage evolution during thermal cycling of Sn-Ag-Cu solders containing antimony, J. Electron. Mater. 50 (3) (2021) 825–841.
[9] S. Ahmed, et al., Effects of aging on SAC-Bi solder materials, in: 15th IEEE Intersociety Conference on Thermal and Thermomechanical Phenomena in Electronic Systems (ITherm), 2016.
[10] Moore, A. and R. Elliott, *Interface undercooling during eutectic solidification.* 1968.
[11] D.W. Henderson, et al., Ag3Sn plate formation in the solidification of near ternary eutectic Sn–Ag–Cu alloys, J. Mater. Res. 17 (11) (2002) 2775–2778.
[12] H.Y. Lu, H. Balkan, K.S. Ng, Effect of Ag content on the microstructure development of Sn-Ag-Cu interconnects, J. Mater. Sci. Mater. Electron. 17 (3) (2006) 171–178.
[13] J. Campbell, The Solidification of Metals, 110, Iron and Steel Institute, Publication, 1968, p. 18.
[14] J. Bromley, F. Vnuk, R. Smith, Mechanical properties of Sn-Ag3Sn alloys, J. Mater. Sci. 18 (10) (1983) 3143–3153.
[15] H. Esaka, K. Shinozuka, M. Tamura, Evolution of Structure Unidirectionally Solidified Sn–Ag3Sn Eutectic Alloy, Mater. Trans. 46 (5) (2005) 916–921.
[16] M. Şahin, E. Çadirli, The effects of temperature gradient and growth rate on the microstructure of directionally solidified Sn–3.5 Ag eutectic solder, J. Mater. Sci. Mater. Electron. 23 (2) (2012) 484–492.
[17] N. Hou, et al., Ag3Sn Morphology Transitions During Eutectic Growth in Sn–Ag Alloys, Metall. Mater. Trans. A (2023).
[18] J.-.M. Song, et al., Crystallization, morphology and distribution of Ag3Sn in Sn–Ag–Cu alloys and their influence on the vibration fracture properties, Mater. Sci. Eng.: A 466 (1–2) (2007) 9–17.
[19] R. Sidhu, N. Chawla, Three-dimensional microstructure characterization of Ag3Sn intermetallics in Sn-rich solder by serial sectioning, Mater. Charact. 52 (3) (2004) 225–230.
[20] R. Sidhu, N. Chawla, Three-dimensional (3D) visualization and microstructure-based modeling of deformation in a Sn-rich solder, Scr. Mater. 54 (9) (2006) 1627–1631.
[21] F. Ochoa, J. Williams, N. Chawla, Effects of cooling rate on the microstructure and tensile behavior of a Sn-3.5 wt.% Ag solder, J. Electron. Mater. 32 (12) (2003) 1414–1420.
[22] F. Ochoa, X. Deng, N. Chawla, Effects of cooling rate on creep behavior of a Sn-3.5 Ag alloy, J. Electron. Mater. 33 (12) (2004) 1596–1607.
[23] J. Keller, et al., Mechanical properties of Pb-free SnAg solder joints, Acta Mater. 59 (7) (2011) 2731–2741.
[24] M. Abtew, G. Selvaduray, Lead-free solders in microelectronics, Mater. Sci. Eng.: R: Rep. 27 (5–6) (2000) 95–141.
[25] E. Dalton, et al., Accelerated temperature cycling induced strain and failure behaviour for BGA assemblies of third generation high Ag content Pb-free solder alloys, Mater. Des. 154 (2018) 184–191.
[26] M.N. Collins, E. Dalton, J. Punch, Microstructural influences on thermomechanical fatigue behaviour of third generation high Ag content Pb-Free solder alloys, J. Alloy. Compd. 688 (2016) 164–170.
[27] S. Xu, et al., Interfacial intermetallic growth and mechanical properties of carbon nanotubes reinforced Sn3.5Ag0.5Cu solder joint under current stressing, J. Alloy. Compd. 595 (2014) 92–102.
[28] W. Plumbridge, C. Gagg, The mechanical properties of lead-containing and lead-free solders—Meeting the environmental challenge, Proc. Inst. Mech. Eng. Part L J. Mater. Des. Appl. 214 (3) (2000) 153–161.
[29] Y. Xu, et al., Intermetallic size and morphology effects on creep rate of Sn-3Ag-0.5 Cu solder, Int. J. Plast. 137 (2021), 102904.
[30] T. Gu, C.M. Gourlay, T.B. Britton, The role of lengthscale in the creep of Sn-3Ag-0.5 Cu solder microstructures, J. Electron. Mater. 50 (3) (2021) 926–938.
[31] K. Kim, S. Huh, K. Suganuma, Effects of cooling speed on microstructure and tensile properties of Sn–Ag–Cu alloys, Mater. Sci. Eng.: A 333 (1–2) (2002) 106–114.
[32] S. Chang, S. Wu, Damping characteristics of Sn–3Ag–0.5 Cu and Sn–37 Pb solders studied by dynamic mechanical analysis, Scr. Mater. 63 (10) (2010) 957–960.
[33] F. Lin, et al., Evolution of Ag3Sn at Sn–3.0 Ag–0.3 Cu–0.05 Cr/Cu joint interfaces during thermal aging, J. Alloy. Compd. 509 (23) (2011) 6666–6672.
[34] S.K. Kang, et al., The microstructure, thermal fatigue, and failure analysis of near-ternary eutectic Sn-Ag-Cu solder joints, Mater. Trans. 45 (3) (2004) 695–702.
[35] K.-.W. Moon, et al., Experimental and thermodynamic assessment of Sn-Ag-Cu solder alloys, J. Electron. Mater. 29 (10) (2000) 1122–1136.
[36] L. Snugovsky, et al., Some aspects of nucleation and growth in Pb free Sn–Ag–Cu solder, Mater. Sci. Technol. 21 (1) (2005) 53–60.
[37] S.K. Kang, et al., Ag3Sn plate formation in the solidification of near-ternary eutectic Sn-Ag-Cu, JOM 55 (6) (2003) 61–65.
[38] S.K. Kang, et al., Controlling Ag3Sn plate formation in near-ternary-eutectic Sn-Ag-Cu solder by minor Zn alloying, JOM 56 (6) (2004) 34–38.
[39] I.E. Anderson, Development of Sn-Ag-Cu and Sn-Ag-Cu-X alloys for Pb-free electronic solder applications, Lead-Free Electron. Solder. (2006) 55–76.
[40] K. Kim, S. Huh, K. Suganuma, Effects of intermetallic compounds on properties of Sn–Ag–Cu lead-free soldered joints, J. Alloy. Compd. 352 (1–2) (2003) 226–236.
[41] S.K. Kang, et al., Formation of AgSn plates in Sn-Ag-Cu alloys and optimization of their alloy composition, in: 53rd Electronic Components and Technology Conference, 2003. Proceedings, IEEE, 2003.
[42] J. Gong, et al., Formation of Ag3Sn plates in SnAgCu solder bumps, Mater. Sci. Eng.: A 527 (10–11) (2010) 2588–2591.
[43] J. Xian, et al., Anisotropic thermal expansion of Ni3Sn4, Ag3Sn, Cu3Sn, Cu6Sn5 and βSn, Intermetallics 91 (2017) 50–64.
[44] H. Ma, et al., In-situ study on growth behavior of Ag3Sn in Sn–3.5 Ag/Cu soldering reaction by synchrotron radiation real-time imaging technology, J. Alloys Compd. 537 (2012) 286–290.
[45] M. Mueller, et al., Morphologies of Primary Cu6Sn5 and Ag3Sn Intermetallics in Sn–Ag–Cu Solder Balls, IEEE Transact. Compon., Packag. Manufact. Technol. 10 (1) (2019) 18–29.
[46] R. Wu, J. Perepezko, Liquidus temperature determination in multicomponent alloys by thermal analysis, Metall. Mater. Trans. A 31 (2) (2000) 497–501.
[47] S. Belyakov, C. Gourlay, Recommended values for the βSn solidus line in Sn-Bi alloys, Thermochim. Acta 654 (2017) 65–69.
[48] J. Xian, et al., Heterogeneous nucleation of Cu6Sn5 in Sn–Cu–Al solders, J. Alloys Compd. 619 (2015) 345–355.
[49] A.-.K. Larsson, L. Stenberg, S. Lidin, The superstructure of domain-twinned η'-Cu6Sn5, Acta Crystallogr., Sect. B: Struct. Sci. 50 (6) (1994) 636–643.
[50] A. Leineweber, C. Wieser, W. Hügel, Crystal structure of incommensurate η''-Cu1. 235Sn intermetallic, Zeitschrift für Kristallographie-Crystalline Materials 235 (10) (2020) 445–457.
[51] A. Leineweber, C. Wieser, W. Hügel, Cu6Sn5 intermetallic: reconciling composition and crystal structure, Scr. Mater. 183 (2020) 66–70.
[52] P.J. Rossi, N. Zotov, E.J. Mittemeijer, Redetermination of the crystal structure of the Ag3Sn intermetallic compound, Zeitschrift für Kristallographie-Crystalline Materials 231 (1) (2016) 1–9.
[53] A. Gangulee, G. Das, M. Bever, An x-ray diffraction and calorimetric investigation of the compound Cu6Sn5, Metall. Trans. 4 (9) (1973) 2063–2066.
[54] G. Zeng, et al., *Solidification of Sn-0.7 Cu-0.15 Zn solder:* in situ *observation*, Metall. Mater. Trans. A 45 (2) (2014) 918–926.
[55] M. Salleh, et al., In situ imaging of microstructure formation in electronic interconnections, Sci. Rep. 7 (1) (2017) 1–11.
[56] J. Xian, et al., Influence of Ni on the refinement and twinning of primary Cu6Sn5 in Sn-0.7 Cu-0.05 Ni, Intermetallics 102 (2018) 34–45.
[57] H. Yu, et al., Defect structures in solution-grown single crystals of the intermetallic compound Ag3Sn, J. Mater. Sci. 53 (7) (2018) 5317–5328.
[58] H.-.W. Chiang, K. Chang, J.-.Y. Chen, The effect of Ag content on the formation of Ag3Sn plates in Sn-Ag-Cu lead-free solder, J. Electron. Mater. 35 (12) (2006) 2074–2080.
[59] F. Gao, H. Nishikawa, T. Takemoto, Intermetallics evolution in Sn-3.5 Ag based lead-free solder matrix on an OSP Cu finish, J. Electron. Mater. 36 (12) (2007) 1630–1634.
[60] V. Vasudevan, et al., Slow cycle fatigue creep performance of Pb-Free (LF) solders, in: Proceedings 57th Electronic Components and Technology Conference, 2007.
[61] *Thermo-Calc Software TCSLD solder alloy solutions database version 4.1.*
[62] J. Nývlt, Kinetics of nucleation in solutions, J. Cryst. Growth 3 (1968) 377–383.
[63] J. Xian, et al., Cu6Sn5 crystal growth mechanisms during solidification of electronic interconnections, Acta Mater. 126 (2017) 540–551.
[64] G. Wanbing, et al., DSC study on the undercooling of droplet solidification of metal melt, Chin. Sci. Bull. 50 (9) (2005) 929.

[65] W.J. Boettinger, M.J. Aziz, Theory for the trapping of disorder and solute in intermetallic phases by rapid solidification, Acta Metall. 37 (12) (1989) 3379–3391.
[66] D.M. Herlach, Dendrite growth kinetics in undercooled melts of intermetallic compounds, Cryst. 5 (3) (2015) 355–375.
[67] L.A. Bendersky, J.W. Cahn, Special grain boundaries based on local symmetries, J. Mater. Sci. 41 (23) (2006) 7683–7690.
[68] Y. Cui, C.M. Gourlay, Growth twinning and morphology of Al45Cr7 and Al13Fe4, J. Alloys Compd. 893 (2022), 162318.
[69] E. Louis, R. Mora, J. Pastor, *Nature of star-shaped clusters of* $FeAl_3$ *in aluminium–iron alloys*, Metal Sci. 14 (12) (1980) 591–594.
[70] G. Zeng, J.W. Xian, C.M. Gourlay, Nucleation and growth crystallography of Al8Mn5 on B2-Al(Mn,Fe) in AZ91 magnesium alloys, Acta Mater. 153 (2018) 364–376.
[71] B. Arfaei, N. Kim, E.J. Cotts, Dependence of Sn grain morphology of Sn-Ag-Cu solder on solidification temperature, J. Electron. Mater. 41 (2) (2012) 362–374.
[72] A.A. Daszki, C.M. Gourlay, On the 3-D shape of interlaced regions in Sn-3Ag-0.5Cu solder balls, J. Electron. Mater. 50 (3) (2021) 808–817.
[73] J. Han, F. Guo, Effects of impurities on double twinning nucleation and grain refinement of Sn-based solder joints, J. Mater. Sci. Mater. Electron. 29 (10) (2018) 8031–8038.
[74] L.P. Lehman, et al., Cyclic twin nucleation in tin-based solder alloys, Acta Mater. 58 (10) (2010) 3546–3556.
[75] Z.L. Ma, et al., Nucleation and twinning in tin droplet solidification on single crystal intermetallic compounds, Acta Mater. 150 (2018) 281–294.
[76] M. Huang, F. Yang, Size effect model on kinetics of interfacial reaction between Sn-xAg-yCu solders and Cu substrate, Sci. Rep. 4 (1) (2014) 1–9.
[77] C. Ho, et al., Theoretical and experimental determination of Cu diffusivity in eutectic Sn–Ag system at 235–280 °C, Thin. Solid. Films 572 (2014) 238–244.
[78] S. Belyakov, C. Gourlay, Heterogeneous nucleation of βSn on NiSn4, PdSn4 and PtSn4, Acta Mater. 71 (2014) 56–68.
[79] Z. Ma, et al., Harnessing heterogeneous nucleation to control tin orientations in electronic interconnections, Nat. Commun. 8 (1) (2017) 1–10.
[80] P. Schumacher, et al., New studies of nucleation mechanisms in aluminium alloys: implications for grain refinement practice, Mater. Sci. Technol. 14 (5) (1998) 394–404.
[81] Y. Cui, et al., Solidification orientation relationships between Al3Ti and TiB2, Acta Mater. 186 (2020) 149–161.
[82] M. Qian, D. StJohn, M. Frost, Heterogeneous nuclei size in magnesium–zirconium alloys, Scr. Mater. 50 (8) (2004) 1115–1119.
[83] G. Peng, Y. Wang, Z. Fan, Competitive heterogeneous nucleation between Zr and MgO particles in commercial purity magnesium, Metall. Mater. Trans. A 49 (6) (2018) 2182–2192.
[84] J. Xian, et al., Nucleation of tin on the Cu6Sn5 layer in electronic interconnections, Acta Mater. 123 (2017) 404–415.
[85] D. Turnbull, Kinetics of heterogeneous nucleation, J. Chem. Phys. 18 (2) (1950) 198–203.